The Astrophysical Journal, 832:148 (22pp), 2016 December 1 doi:10.3847/0004-637X/832/2/148

MOLECULAR GAS ALONG A BRIGHT Hα FILAMENT IN 2A 0335+096 REVEALED BY ALMA

A. N. Vantyghem[1], B. R. McNamara[1,2], H. R. Russell[3], M. T. Hogan[1,2], A. C. Edge[4], P. E. J. Nulsen[5,6], A. C. Fabian[3], F. Combes[7,8], P. Salomé[7], S. A. Baum[9], M. Donahue[10], R. A. Main[11], N. W. Murray[11], R. W. O'Connell[12], C. P. O'Dea[9], J. B. R. Oonk[13,14], I. J Parrish[11], J. S. Sanders[15], G. Tremblay[16], and G. M. Voit[10]
[1] Department of Physics and Astronomy, University of Waterloo, Waterloo, ON N2L 3G1, Canada; a2vantyg@uwaterloo.ca
[2] Perimeter Institute for Theoretical Physics, Waterloo, Canada
[3] Institute of Astronomy, Madingley Road, Cambridge CB3 0HA, UK
[4] Department of Physics, Durham University, Durham DH1 3LE, UK
[5] Harvard-Smithsonian Center for Astrophysics, 60 Garden Street, Cambridge, MA 02138, USA
[6] ICRAR, University of Western Australia, 35 Stirling Hwy, Crawley, WA 6009, Australia
[7] LERMA, Observatoire de Paris, CNRS, UPMC, PSL Univ., 61 avenue de l'Observatoire, 75014 Paris, France
[8] Collège de France, 11 place Marcelin Berthelot, 75005, Paris
[9] Department of Physics and Astronomy, University of Manitoba, Winnipeg, MB R3T 2N2, Canada
[10] Department of Physics and Astronomy, Michigan State University, 567 Wilson Road, East Lansing, MI 48824, USA
[11] Canadian Institute for Theoretical Astrophysics, University of Toronto, 60 St. George Street, Toronto, ON M5S 3H8, Canada
[12] Department of Astronomy, University of Virginia, P.O. Box 400235, Charlottesville, VA 22904, USA
[13] ASTRON, the Netherlands Institute for Radio Astronomy, Postbus 2, NL-7990 AA Dwingeloo, The Netherlands
[14] Leiden Observatory, Leiden University, P.O. Box 9513, NL-2300 RA Leiden, The Netherlands
[15] Max-Planck-Institut für extraterrestrische Physik, Giessenbachstrasse 1, D-85748 Garching, Germany
[16] Department of Physics and Yale Center for Astronomy & Astrophysics, Yale University, 217 Prospect Street, New Haven, CT 06511, USA
Received 2016 August 31; revised 2016 September 29; accepted 2016 October 1; published 2016 November 29

ABSTRACT

We present ALMA CO(1–0) and CO(3–2) observations of the brightest cluster galaxy (BCG) in the 2A 0335+096 galaxy cluster ($z = 0.0346$). The total molecular gas mass of $1.13 \pm 0.15 \times 10^9\,M_\odot$ is divided into two components: a nuclear region and a 7 kpc long dusty filament. The central molecular gas component accounts for $3.2 \pm 0.4 \times 10^8\,M_\odot$ of the total supply of cold gas. Instead of forming a rotationally supported ring or disk, it is composed of two distinct, blueshifted clumps south of the nucleus and a series of low-significance redshifted clumps extending toward a nearby companion galaxy. The velocity of the redshifted clouds increases with radius to a value consistent with the companion galaxy, suggesting that an interaction between these galaxies <20 Myr ago disrupted a pre-existing molecular gas reservoir within the BCG. Most of the molecular gas, $7.8 \pm 0.9 \times 10^8\,M_\odot$, is located in the filament. The CO emission is co-spatial with a 10^4 K emission-line nebula and soft X-rays from 0.5 keV gas, indicating that the molecular gas has cooled out of the intracluster medium over a period of 25–100 Myr. The filament trails an X-ray cavity, suggesting that the gas has cooled from low-entropy gas that has been lifted out of the cluster core and become thermally unstable. We are unable to distinguish between inflow and outflow along the filament with the present data. Cloud velocities along the filament are consistent with gravitational free-fall near the plane of the sky, although their increasing blueshifts with radius are consistent with outflow.

Key words: galaxies: active – galaxies: clusters: individual (2A 0335+096) – galaxies: ISM – galaxies: kinematics and dynamics

1. INTRODUCTION

Located at the centers of galaxy clusters, brightest cluster galaxies (BCGs) are the largest and most luminous galaxies in the universe. They are giant elliptical galaxies with extended stellar envelopes and predominantly old, "red and dead" stellar populations. However, BCGs situated in cooling flow clusters (Fabian 1994), where the cooling time of the hot gas is shorter than the age of the system, harbour upward of $10^9\,M_\odot$ of molecular gas, approaching $10^{11}\,M_\odot$ in the most extreme systems (Edge 2001; Salomé & Combes 2003). Star formation proceeding at rates of several to tens of solar masses per year, which exceeds the star formation rates of many spiral galaxies, is also observed in these systems (McNamara 2004; O'Dea et al. 2008; McDonald et al. 2011; Donahue et al. 2015; Tremblay et al. 2015).

Molecular clouds and stars in BCGs likely form from the cooling of the hot intracluster medium (ICM). Correlations between star formation rate and the rate of mass deposition from the ICM support this picture (Egami et al. 2006; O'Dea et al. 2008). Furthermore, cold gas and star formation are observed almost exclusively in systems where the central cooling time is below a sharp threshold of $\sim 5 \times 10^8$ years (Rafferty et al. 2008), or equivalently where the entropy is less than 30 keV cm^2 (Cavagnolo et al. 2008; Voit et al. 2008). This threshold has been attributed to the onset of thermal instabilities in the ICM (Gaspari et al. 2012; Voit & Donahue 2015). These systems also host diffuse emission-line nebulae, which are likely the ionized skins of molecular clouds (Heckman 1981; Hu et al. 1985; O'Dea et al. 1994; Jaffe et al. 2005; Oonk et al. 2010). Alternatively, the peculiar emission line ratios in BCGs (e.g., Heckman et al. 1989) may originate from primarily neutral gas that is excited by collisions with energetic particles (Ferland et al. 2009).

Although the reservoirs of molecular gas observed in BCGs are quite massive, they constitute only a few percent of the mass expected from unimpeded cooling (Peterson & Fabian 2006). Instead, feedback from the active galactic nucleus (AGN) is heating the ICM and regulating the rate of cooling (McNamara & Nulsen 2007, 2012; Fabian 2012).

High-resolution *Chandra* X-ray imaging of cool core clusters shows that AGNs launch jets that inflate cavities, drive shock fronts, and generate sound waves, offsetting radiative losses from the ICM (e.g., McNamara et al. 2000; Blanton et al. 2001; Fabian et al. 2006). The rate of heating is closely tied to the rate of cooling in a large sample of groups and clusters (Bîrzan et al. 2004; Dunn & Fabian 2006; Rafferty et al. 2006), and is sufficient to prevent the bulk of the hot gas from cooling.

Accretion of molecular gas potentially plays a key role in forming a feedback loop, as it connects residual cooling of the ICM with energetic outbursts from the AGN (e.g., Pizzolato & Soker 2005; Gaspari et al. 2013; Li & Bryan 2014a). While the effects of AGN feedback on the hot atmosphere are clear, little is known about its connection to the cold gas. Radio jets are known to couple to emission-line nebulae, driving outflows of ionized (Morganti et al. 2005; Nesvadba et al. 2006; Villar-Martín et al. 2006) and molecular gas (Alatalo et al. 2011; Morganti et al. 2015) in radio galaxies. NGC1275, at the center of the Perseus cluster, hosts a filamentary Hα nebula with two prominent filaments extending toward an X-ray cavity (Fabian et al. 2003), suggesting that the filaments have been drawn out of a central reservoir. These filaments are well correlated with soft X-ray emission as well as molecular hydrogen (Lim et al. 2012) and CO (Salomé et al. 2006, 2011). Infalling molecular gas toward the center of the BCG suggests that the uplifted gas is returning in a molecular "fountain" (Lim et al. 2008). Narrow, redshifted absorption lines have been observed in NGC5044 (David et al. 2014) and A2597 (Tremblay et al. 2016), indicating that molecular clouds are inflowing toward the central black hole. ALMA Early Science observations of A1835 revealed $10^{10}\,M_{\odot}$ of molecular gas being uplifted by the X-ray cavities in a bipolar outflow (McNamara et al. 2014). PKS0745-191 harbours an even more dramatic outflow—virtually all of its molecular gas has been swept from the BCG in three low-velocity filaments (Russell et al. 2016). These results have led McNamara et al. (2016) to postulate that molecular gas condenses out of low-entropy ICM that is lifted from the cluster center by X-ray cavities.

Here we present ALMA Cycle 1 observations of the molecular gas in the BCG of 2A 0335+096 (also known as RXJ0338+09), traced by CO(1–0) and CO(3–2) line emission. 2A 0335+096 is one of the brightest X-ray objects on the sky (Edge et al. 1990; Reiprich & Böhringer 2002), and has a center with a short radiative cooling time (Schwartz et al. 1980; Singh et al. 1986, 1988; White et al. 1991). Its X-ray atmosphere is complex, containing a series of cool clumps (Mazzotta et al. 2003; Werner et al. 2006), a cold front that was likely induced by sloshing motions (Mazzotta et al. 2003; Sanders et al. 2009), and several cavities corresponding to multiple generations of AGN feedback with a total enthalpy of 5×10^{59} erg (Sanders et al. 2009). Multiphase gas in the ICM traces an extended Hα filament within the BCG with a total luminosity of $L_{\mathrm{H}\alpha} = 8 \times 10^{41}\,\mathrm{erg\,s^{-1}}$ (Romanishin & Hintzen 1988; Donahue et al. 2007; Sanders et al. 2009). Farage et al. (2012) argued that the Hα filament consists of a 2 kpc, counterrotating disk within the 17 kpc filament. Single-dish IRAM-30 m observations detected the 2A 0335+096 BCG at CO(1–0), measuring a total molecular gas mass of $2.7 \pm 0.3 \times 10^{9}\,M_{\odot}$ (Edge & Frayer 2003, corrected for cosmology). Optical, UV, and IR observations of the BCG show ongoing star formation at a rate of several solar masses per year (Romanishin & Hintzen 1988; Donahue et al. 2007; O'Dea et al. 2008). X-ray spectroscopy from *Chandra* and *XMM-Newton* indicate that the 0.5 keV gas within the ICM is cooling out of the hot atmosphere and depositing mass onto the BCG at $<30\,M_{\odot}\,\mathrm{yr^{-1}}$ (Sanders et al. 2009). The ALMA observations presented here resolve the spatial and velocity structure of the molecular gas within the BCG, revealing a striking correlation between molecular gas and the Hα filament.

Throughout this paper we assume a standard Λ-CDM cosmology with $H_0 = 70\,\mathrm{km\,s^{-1}\,Mpc^{-1}}$, $\Omega_{\mathrm{m},0} = 0.3$, and $\Omega_{\Lambda,0} = 0.7$. At the redshift of 2A 0335+096 ($z = 0.0346$; McNamara et al. 1990), the angular scale is $1'' = 700$ pc and the luminosity distance is 150 Mpc. This paper is organized as follows. Details of the ALMA observations and data reduction are given in Section 2. Our results pertaining to the morphological and kinematic distribution of the molecular gas and its relation to other wavelengths are described in Section 3. The origin of the molecular gas is discussed in Section 4, and the main results are summarized in Section 5.

2. OBSERVATIONS AND DATA REDUCTION

The BCG in the 2A 0335+096 galaxy cluster (R.A.: 03:38:40.50, decl.: +09:58:12.3) was observed by ALMA Cycle 1 (Program ID 2012.1.00837.S, PI McNamara) centered at 111.394 GHz and 334.169 GHz to cover the CO(1–0) and CO(3–2) lines. The CO(1–0) observation was divided into two blocks, which were observed in band 3 on 2014 July 22 and 2015 March 08. Both observations had an on-source integration time of 35 minutes. For the 2014 July (2015 March) observation the array was configured with 33 (30) antennas with baselines of 17–716 m (12–280 m), each with a primary beam diameter of $56''$. Our observations employed the frequency division correlator mode, so had a frequency resolution of 488.281 kHz ($1.31\,\mathrm{km\,s^{-1}}$) over a 1.875 GHz bandwidth. The CO(3–2) line was observed in band 7 with one 30 minute on-source integration on 2014 August 12. The observation used 34 antennas with baselines of 19–915 m and a primary beam of $18.''5$. At CO(3–2) the velocity resolution in frequency division correlator mode was $0.44\,\mathrm{km\,s^{-1}}$. Velocity channels were binned together during imaging to improve sensitivity. An additional baseband with 2 GHz bandwidth was included in order to image the continuum.

The observations were primarily calibrated in CASA version 4.4.0 (McMullin et al. 2007) using the automatic pipeline scripts. Additional phase self-calibration on the nuclear continuum improved the signal-to-noise of the CO(1–0) observation by a factor of 1.2. The nuclear continuum flux at CO(3–2) was too faint to perform successful self-calibration.

The phase calibrator chosen automatically at the time of the 2015 March CO(1–0) observation was located 10° away from 2A 0335+096 and had a flux 10 times fainter than the calibrator used in the 2014 July CO(1–0) observation. The resulting phase solutions determined by the pipeline were poor, and a manual recalibration of the data did not improve these solutions to an acceptable level. The phase self-calibration also did not rectify the problem. We therefore do not include this observation in our analysis.

Images of the continuum were created for each band by imaging the line-free channels. An unresolved point source was detected in each image. At 109.84 GHz the nuclear continuum flux is 6.854 ± 0.044 mJy in the 2014 July observation and 6.36 ± 0.15 mJy in the 2015 March observation. This implies a

variability of 7.2% ± 2.3% over an eight-month period, which is consistent with the variability seen in other BCGs with active cores (Hogan et al. 2015). At 335.12 GHz (2014 August) the nuclear continuum flux is 1.14 ± 0.15 mJy. The corresponding spectral index, following the convention $S_\nu \propto \nu^{-\alpha}$ and considering only the 2014 observations, is $\alpha = 1.61 \pm 0.27$. The location of the continuum source is consistent with 5 GHz VLBI (Sanders et al. 2009). No continuum emission is associated with the nearby companion galaxy. Imaging the continuum in narrow velocity channels (3 km s^{-1}) shows no evidence of line absorption against the continuum emission.

Images of line emission were reconstructed using CLEAN with a Briggs weighting of 2. No continuum subtraction was applied to the CO(3–2) observation, as the continuum flux is small compared to the line emission. The resulting images had a synthesized beam of $1\farcs3 \times 0\farcs92$ (PA $-34\fdg5$) at CO(1–0) and $0\farcs39 \times 0\farcs23$ (PA $-50\fdg0$) at CO(3–2). The rms noise in 20 km s^{-1} line-free channels was 0.56 mJy beam^{-1} and 0.61 mJy beam^{-1} at CO(1–0) and CO(3–2), respectively. In regions of low signal-to-noise we further bin the spectra to either 40 km s^{-1} or 60 km s^{-1} channels, as needed. Missing short spacings will filter out emission on spatial scales larger than ∼11″ at CO(1–0) and ∼3″ at CO(3–2).

A reference velocity of 10368 km s^{-1} ($z = 0.0346$) was adopted for this analysis. This is a stellar absorption measurement of the BCG that was measured by Huchra. The result was first published in (McNamara et al. 1990, quoting private communication with Huchra) and subsequently in the 2MASS catalog (Lavaux & Hudson 2011; Huchra et al. 2012), who quote an uncertainty of 10 km s^{-1}. The center of the CO (1–0) and CO(3–2) emission is better estimated by the adopted systemic velocity than by the redshifts adopted by previous studies. For reference, a redshift of $z = 0.0349$, which is used by Donahue et al. (2007) and Farage et al. (2012), corresponds to a velocity of +92 km s^{-1} in our adopted frame.

3. RESULTS

3.1. Distribution of Molecular Gas

The *Hubble Space Telescope* (*HST*) WFPC2 F606W image presented in the middle frame of Figure 1 shows the central 28 × 28 kpc of the galaxy cluster, encompassing the BCG and a nearby companion galaxy that is situated 5 kpc in projection from the BCG and well within its light profile. Stellar absorption lines from the two galaxies indicate that the companion is offset from the BCG by 212 ± 58 km s^{-1} in velocity space (Gelderman 1996). This low velocity suggests that the radial distance between the galaxies is small, so the companion is not just a chance projection. However, this information is not sufficient to determine the true 3D distance or relative velocity between the BCG and companion. Outside of the shown field of view, the closest galaxies are 25 kpc and 28 kpc from the BCG, respectively. These both lie well beyond the molecular gas, so are unlikely to be relevant in our analysis.

Maps of the integrated CO(1–0) and CO(3–2) flux are presented alongside the *HST* image in Figure 1. These maps were created by summing the flux in each pixel over the velocity range −500 to 500 km s^{-1}, which encompasses all of the observed flux (see Figure 2). The maps have been corrected for the response of the primary beam, with contour levels

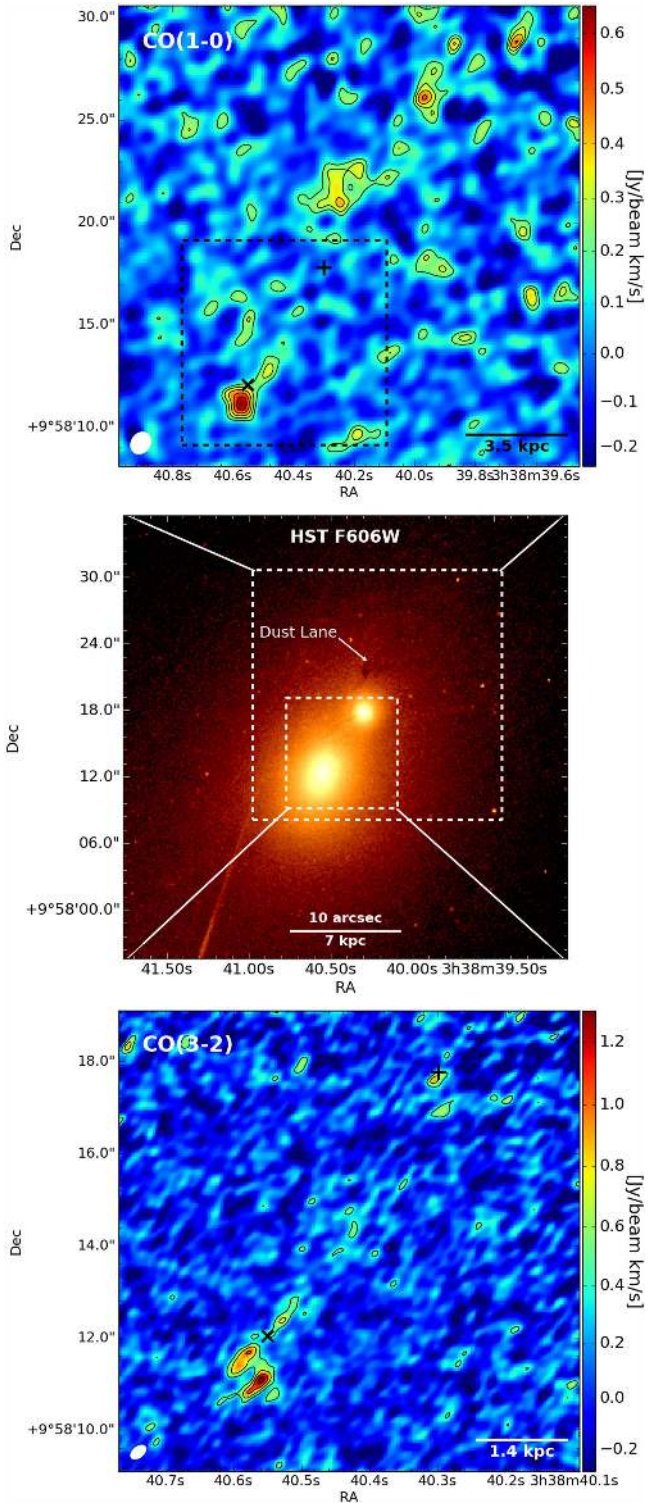

Figure 1. Top: integrated flux of the CO(1–0) ALMA image. The contours are −2, 2, 3, 4, 5σ,..., where $\sigma = 0.095$ Jy beam^{-1} km s^{-1}. The × indicates the position of a radio AGN determined from VLBI (Sanders et al. 2009), and the + indicates the flux centroid of the companion galaxy determined from the *HST* F606W image. The 1.13 × 0.92 arcsec (PA −35°) synthesized beam is shown in white in the lower left corner. The box indicates the CO(3–2) frame shown in the bottom panel. Middle: *HST* WFPC2 F606W optical image of the 2A 0335+096 BCG and the nearby companion galaxy. Bottom: integrated flux of the CO(3–2) ALMA image, with contours set at −3, 3, 5, 7, and 9σ, where $\sigma = 0.145$ Jy beam^{-1} km s^{-1}. The 0.32 × 0.20 arcsec beam is shown in white in the lower left corner.

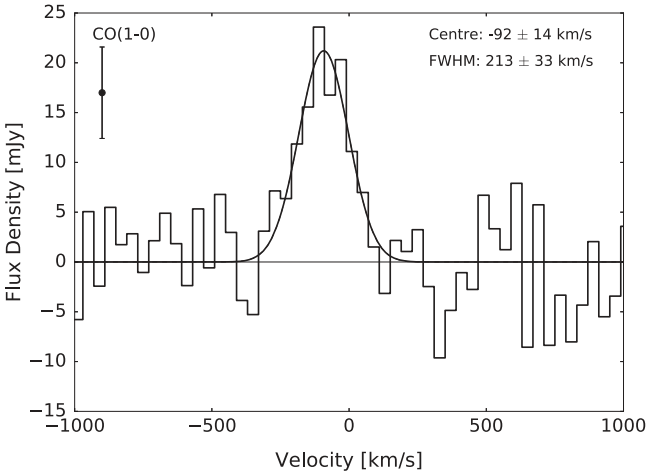

Figure 2. CO(1–0) spectrum extracted from a $17\farcs5 \times 22''$ box that encompasses both the BCG and the extended filament. The best-fit parameters are given in Table 1. The error bar indicates the rms variation in the line-free channels.

determined from the line-free regions of an uncorrected map. Significant CO emission is observed in two primary locations: near the nucleus of the BCG and in a filament situated beyond a nearby companion galaxy. The filament falls outside of the CO (3–2) field of view.

Figure 2 shows the CO(1–0) spectrum extracted from a $17\farcs5 \times 22''$ (12.3 × 15.4 kpc) box encompassing all of the observed flux. This region is similar in size to the $21\farcs5$ IRAM 30 m beam. The spectrum was well-fit by a single Gaussian component centered at $-92 \pm 14\,\mathrm{km\,s^{-1}}$ with a linewidth of $213 \pm 33\,\mathrm{km\,s^{-1}}$ (full width at half maximum; FWHM). Spectral fitting throughout this work used the LMFIT[17] package with one to three Gaussian components, as necessary. Each spectrum has been corrected for the response of the primary beam as well as instrumental broadening introduced by the velocity binning. Table 1 lists the best-fitting parameters for all spectra.

The total CO(1–0) flux recovered by these observations is $4.8 \pm 0.6\,\mathrm{Jy\,km\,s^{-1}}$, which is consistent with the OVRO measurement of $7.1 \pm 2.4\,\mathrm{Jy\,km\,s^{-1}}$ within 2σ (Edge & Frayer 2003). This flux constitutes $43 \pm 7\%$ of the IRAM 30 m flux ($11.4 \pm 1.1\,\mathrm{Jy\,km\,s^{-1}}$; Edge 2001), implying that over half of the molecular gas is undetected in our observations. Similar recovered fractions were noted in ALMA observations of NGC5044 (David et al. 2014) and A1664 (Russell et al. 2014). Missing short spacings filter out emission on scales larger than 11 arcsec at CO(1–0) or 3 arcsec at CO(3–2).

3.1.1. Gas in the BCG

Near the nucleus of the BCG the molecular gas is distributed among a series of clumps of varying size. At CO(1–0) the emission is mostly concentrated in an unresolved clump located south of the nucleus. At CO(3–2) this feature is further resolved into two clumps of comparable size. The brighter of these clumps is coincident with significant dust extinction in the optical imaging, which is discussed further in Section 3.5. No molecular gas is concentrated at the location of the AGN. Toward the northwest the CO emission extends in a small spur that breaks into a series of small, faint clouds. These clouds are distributed in the direction of a nearby companion galaxy that itself hosts a small association of molecular gas.

A spectrum was extracted from a $4\farcs5 \times 4\farcs5$ box centered on the nucleus at both CO(1–0) (Figure 3 top) and CO(3–2) (Figure 4). This regions includes all of the southern emission and most of the clouds to the northwest. Both spectra are best fit by two Gaussian components, with one blueshifted to $\sim -200\,\mathrm{km\,s^{-1}}$ and one redshifted to $\sim 100\,\mathrm{km\,s^{-1}}$ with respect to the systemic stellar velocity of the BCG. The total integrated flux in this region is $1.36 \pm 0.17\,\mathrm{Jy\,km\,s^{-1}}$ at CO(1–0).

Additional spectra were extracted for the distinct structures within the BCG. At CO(1–0) these include the southern unresolved clump as well as the spur extending to the northwest, which are identified in Figure 5. The resulting spectra are shown in the bottom panels of Figure 6. Both are well-fit by a single velocity component that, when combined, accounts for the two peaks observed in the total BCG spectrum in Figure 3. The blueshifted emission is observed exclusively in the southern clump, while the spur to the northwest is entirely redshifted. Both are relatively broad, with FWHM of $297 \pm 38\,\mathrm{km\,s^{-1}}$ and $238 \pm 43\,\mathrm{km\,s^{-1}}$, respectively.

These regions can be subdivided further at CO(3–2), as shown in Figure 7. The "South BCG" region is the same as in CO(1–0) (Figure 5) to allow for a direct comparison, but has also been split into two regions that are not shown in the figure, one for each clump. Toward the northwest the emission has also been divided into two regions based on distance from the nucleus. Neither of these regions corresponds 1:1 with the "North BCG" region in Figure 5, which extends midway into the "Diffuse Gas" region. All CO(3–2) spectra are shown in Figure 8, with all fit parameters listed in Table 1. Multiple velocity components are required for several of the spectra. In the northwestern regions most of the linewidths are narrow ($<100\,\mathrm{km\,s^{-1}}$), so the multiple peaks likely arise from giant molecular clouds or associations of different velocities. South of the BCG, multiple velocity components are only required to fit the larger of the two clumps, lying to the southwest. This clump is coincident with dust extinction, although the north-eastern clump may still be coincident with dust if it is located on the far side of the BCG.

3.1.2. Filament

Beyond the companion galaxy the molecular gas is located in a 7 kpc long filament that is coincident with an extended region of significant dust extinction. Most of the emission is localized in the inner portion of the filament, with a second, smaller region at the filament tail reaching 5σ significance. These two regions are connected by a faint channel that is not evident in Figure 1, but is significantly detected in the maps presented in Section 3.3. This is because the channel has a narrow linewidth, so is drowned out by the noise when integrated between -500 and $500\,\mathrm{km\,s^{-1}}$. Figure 3 (bottom) shows the CO(1–0) spectrum of the filament extracted from an $8'' \times 8\farcs5$ box. We are unable to obtain a CO(3–2) spectrum of the filament because it lies outside of the field of view. The CO (1–0) spectrum is well-fit by a single Gaussian component with an integrated flux of $3.3 \pm 0.4\,\mathrm{Jy\,km\,s^{-1}}$, which is more than double the integrated flux within the BCG.

Spectra of the inner and outer clumps in the filament are shown in Figure 6, with the regions identified in Figure 5. Two velocity components are significantly detected in the inner

[17] https://lmfit.github.io/lmfit-py/

Table 1
Parameters of Molecular Features

CO Line	Region	χ^2/dof	Velocity Center (km s^{-1})	FWHM (km s^{-1})	Integrated Intensity (Jy km s^{-1})	Gas Mass ($10^8\,M_\odot$)
$J = 1$–0	Total	101/107	-92 ± 14	213 ± 33	4.8 ± 0.6	11.3 ± 1.5
	BCG	154/67	-219 ± 21	266 ± 57	0.73 ± 0.13	1.7 ± 0.3
			109 ± 12	164 ± 32	0.63 ± 0.11	1.5 ± 0.3
	Filament	132/107	-96 ± 11	196 ± 25	3.3 ± 0.4	7.8 ± 0.9
	South BCG	136/107	-172 ± 16	297 ± 38	0.99 ± 0.11	2.33 ± 0.26
	North BCG	131/107	134 ± 18	238 ± 43	0.560 ± 0.088	1.31 ± 0.21
	Inner filament	291/214	-28.1 ± 3.6	100.9 ± 8.8	1.22 ± 0.09	2.86 ± 0.21
			-164.7 ± 3.0	34.5 ± 8.1	0.32 ± 0.06	0.74 ± 0.14
	Outer filament	240/211	-132.0 ± 3.4	55.6 ± 8.6	0.75 ± 0.10	1.77 ± 0.23
			-258.3 ± 8.1	51 ± 21	0.27 ± 0.10	0.64 ± 0.22
			-31.6 ± 6.9	38 ± 19	0.22 ± 0.09	0.51 ± 0.21
$J = 3$–2	BCG	54/34	-223 ± 15	188 ± 36	4.8 ± 0.8	1.60 ± 0.28
			121 ± 27	282 ± 71	4.7 ± 1.0	1.58 ± 0.33
	South BCG	108/74	-160 ± 10	279 ± 17	6.37 ± 0.45	2.14 ± 0.15
			-281.1 ± 3.5	73 ± 11	1.5 ± 0.3	0.50 ± 0.10
	South BCG: NE Clump	80/77	-201.4 ± 7.6	275 ± 18	2.46 ± 0.14	0.83 ± 0.05
	South BCG: SW Clump	65/74	-147 ± 19	300 ± 32	1.92 ± 0.23	0.64 ± 0.08
			-278.6 ± 3.2	77 ± 10	0.89 ± 0.16	0.30 ± 0.05
	BCG Spur	83/74	127 ± 24	368 ± 67	3.1 ± 0.5	1.03 ± 0.16
			93.5 ± 7.4	79 ± 23	0.95 ± 0.36	0.32 ± 0.12
	Diffuse Gas	32/34	188.3 ± 4.9	117 ± 13	2.56 ± 0.23	0.86 ± 0.08
			22.2 ± 8.2	46 ± 30	0.45 ± 0.22	0.15 ± 0.08
	Companion Galaxy	36/37	224 ± 19	256 ± 46	1.65 ± 0.25	0.56 ± 0.09

Note. All spectra have been corrected for the response of the primary beam and instrumental broadening. Masses determined from the CO(3–2) line have been calculated assuming CO(3–2)/CO(1–0) = 7.

filament. They are slightly blueshifted with respect to the BCG, with the primary component moving at $-28.1 \pm 3.6\,\mathrm{km\,s^{-1}}$ and the secondary at $-164.7 \pm 3.0\,\mathrm{km\,s^{-1}}$. The outer filament consists of three velocity components, moving at $-31.6 \pm 6.9\,\mathrm{km\,s^{-1}}$, $-132.0 \pm 3.4\,\mathrm{km\,s^{-1}}$, and $-258.3 \pm 8.1\,\mathrm{km\,s^{-1}}$. The primary component is the central line, which is blueshifted by $100\,\mathrm{km\,s^{-1}}$ relative to the main peak in the inner filament. Along the entire filament the broadest component is the primary peak in the inner filament, which still has a linewidth of only $101 \pm 9\,\mathrm{km\,s^{-1}}$ FWHM. All of the other peaks have widths in the range of 30–60 $\mathrm{km\,s^{-1}}$. These linewidths are much narrower than for the gas in the BCG, reflecting the depth of the underlying gravitational potential.

3.1.3. Companion Galaxy

A small clump of gas detected in CO(3–2) is coincident with the nucleus of the companion galaxy. This emission lies within the noise of the CO(1–0) data. The clump is also unresolved at CO(3–2), so spreading the total flux over the larger CO(1–0) beam will decrease the observed brightness. A single-Gaussian fit to its CO(3–2) spectrum, shown in Figure 8, shows that the gas is redshifted to $224 \pm 19\,\mathrm{km\,s^{-1}}$ with respect to the systemic stellar component of the BCG. This is consistent with its stellar velocity of $212 \pm 58\,\mathrm{km\,s^{-1}}$, implying that the molecular gas is bound to the companion galaxy. This molecular gas linewidth of $256 \pm 46\,\mathrm{km\,s^{-1}}$ FWHM is fairly typical of small elliptical galaxies, so the molecular gas may be virialized within the galaxy. Following the mass conversion discussed in Section 3.2 and assuming a line flux ratio of CO(3–2)/CO(1–0) ≈ 7, the total molecular gas mass within the companion galaxy is $5.6 \pm 0.9 \times 10^7\,M_\odot$.

3.2. Molecular Gas Mass

The integrated flux of the CO(1–0) line ($S_{\mathrm{CO}}\Delta v$) can be converted to a molecular gas mass, assuming a constant CO-to-H_2 conversion factor (X_{CO}), according to the equation (Solomon et al. 1987; Solomon & Vanden Bout 2005; Bolatto et al. 2013)

$$M_{\mathrm{mol}} = 1.05 \times 10^4 X_{\mathrm{CO,Gal}} \left(\frac{S_{\mathrm{CO}}\Delta v\, D_L^2}{1+z} \right) M_\odot. \quad (1)$$

Here $S_{\mathrm{CO}}\Delta v$ is expressed in $\mathrm{Jy\,km\,s^{-1}}$, D_L is the luminosity distance in Mpc, and z is the redshift of the BCG. We assume a Galactic CO-to-H_2 conversion factor, $X_{\mathrm{CO,gal}} = 2 \times 10^{-20}\,\mathrm{cm^{-2}}\,(\mathrm{K\,km\,s^{-1}})^{-1}$, which is typical of molecular clouds in the disk of the Milky Way. However, the conversion factor is not universal. In particular, low-metallicity regions tend to have high values of X_{CO}. The Galactic conversion factor can be approximately applied down to metallicities of $\sim 0.5\,Z_\odot$ (Bolatto et al. 2013). In 2A 0335+096, the metallicity inferred from the ICM peaks at $0.95 \pm 0.06\,Z_\odot$ at the cluster center (Sanders et al. 2009), so the Galactic X_{CO} should be appropriate. On the other hand, LIRG and starburst galaxies are known to have very low values of X_{CO}. However, the *Spitzer*-derived total IR luminosity of the BCG, $6.7 \times 10^9\,L_\odot$ (Donahue et al. 2011), is well below the $10^{11}\,L_\odot$ threshold for a LIRG. Narrow absorption features observed in NGC5044 (David et al. 2014) and A2597 (Tremblay et al. 2016) suggest that molecular clouds in BCGs have similar linewidths to those of the Milky Way. We therefore expect that the Galactic value is appropriate here. Our

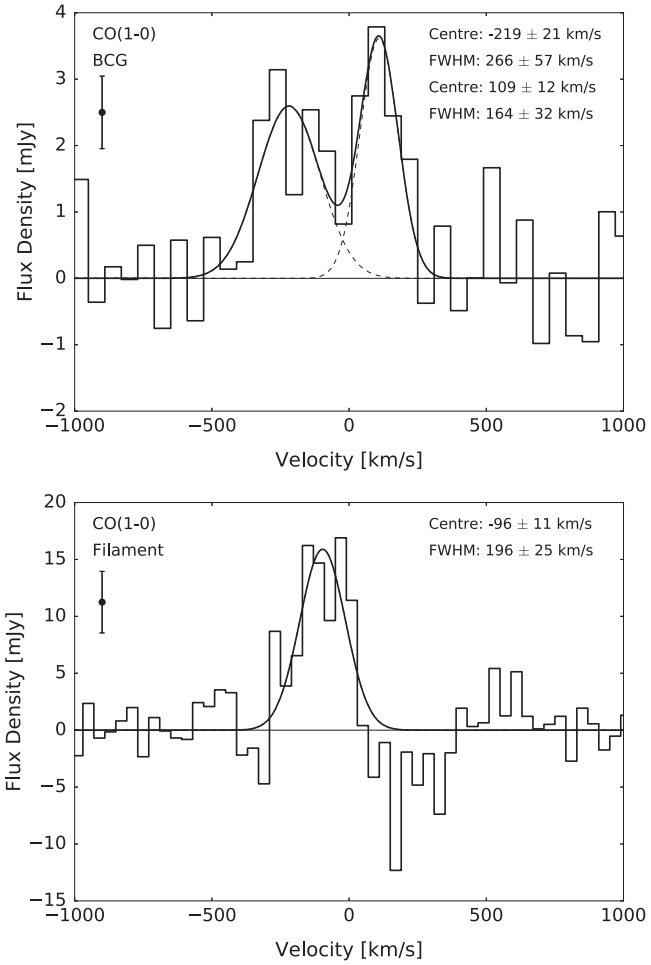

Figure 3. CO(1–0) spectra from a $4\farcs5 \times 4\farcs5$ box centered on the BCG (top) and an $8'' \times 8\farcs5$ box enclosing the filament (bottom). The spectra are each fit by one or two Gaussian components, and the best-fit parameters are given in Table 1. The error bars indicate the rms variation in the line-free channels.

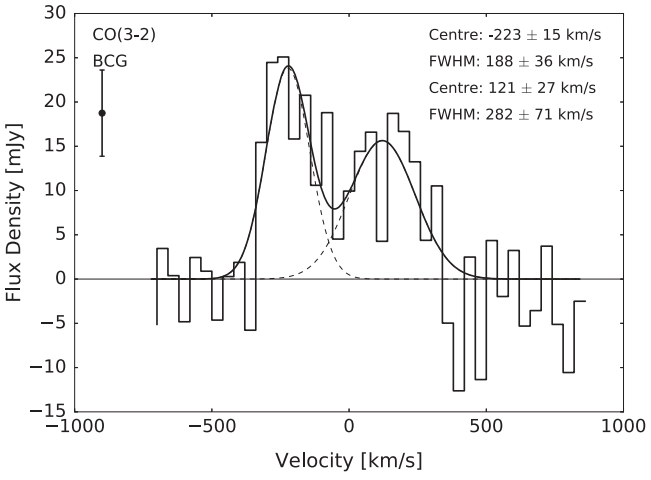

Figure 4. CO(3–2) spectrum of the BCG extracted from the same region as Figure 3 (top panel). The best-fit parameters are given in Table 1. The error bar indicates the rms variation in the line-free channels.

broad conclusions are not affected by a factor of few difference in the adopted conversion factor.

The total CO(1–0) flux detected in our observations, $4.8 \pm 0.6\,\mathrm{Jy\,km\,s^{-1}}$, corresponds to a molecular gas mass of

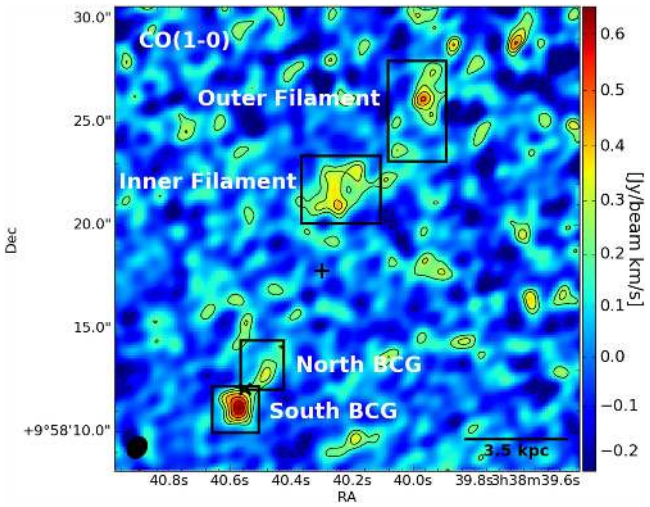

Figure 5. CO(1–0) integrated intensity map identifying regions with distinct molecular gas features. The spectra associated with these regions are shown in Figure 6. The field of view is $22''$ (15.4 kpc) on a side, showing the same area as in Figure 1. The $\times$ and $+$ indicate the centroids of the BCG and companion galaxy, respectively.

$1.13 \pm 0.15 \times 10^9\,M_\odot$. Of this, $3.2 \pm 0.4 \times 10^8\,M_\odot$ is localized to the BCG and $7.8 \pm 0.9 \times 10^8\,M_\odot$ is contained in the elongated filament north of the companion galaxy. Table 1 lists the molecular gas mass associated with each CO(1–0) spectrum.

Masses are derived from CO(3–2) assuming a constant CO (3–2)/CO(1–0) flux ratio. This ratio was determined by smoothing the CO(3–2) data cube to the CO(1–0) resolution and extracting the spectrum from a 5×5 arcsec box centered on the BCG for each line. The spectra were each fitted with two Gaussian components. Summing the fluxes of each component, the resulting flux ratio is $\mathrm{CO(3\text{–}2)/CO(1\text{–}0)} = 7.2 \pm 1.4$. We therefore adopt a factor of 7 difference between the two integrated fluxes, with the caveat that the conversion is only accurate to ~20%. The ratio of integrated brightness temperature (in units of $\mathrm{K\,km\,s^{-1}}$) is 0.80 ± 0.16. For optically thick CO emission this ratio indicates that the gas is approximately thermalized, implying gas densities above $10^4\,\mathrm{cm^{-3}}$.

3.3. Velocity Distribution

In order to study the velocity structure of the molecular gas, we extracted spectra from each pixel of the datacube averaged over a box the size of the synthesized beam. Each spectrum was fit with a single Gaussian component. The significance of the line was tested using a Monte Carlo analysis following the prescription of Protassov et al. (2002, see Section 5.2), with detections requiring a 2σ significance. Spectra containing a line detection were then tested with a second component following the same prescription. The resulting velocity (centroid and FWHM) maps are presented alongside the integrated flux for the corresponding component in Figures 9 and 10 for CO(1–0) and CO(3–2), respectively. The CO(1–0) maps were created with $40\,\mathrm{km\,s^{-1}}$ bins, with each pixel additionally tested with $20\,\mathrm{km\,s^{-1}}$ bins to ensure that the narrow features toward the tail of the filament could be recovered. $20\,\mathrm{km\,s^{-1}}$ velocity bins were used for the CO(3–2) map. The maps have been overlaid with the corresponding contours from Figure 1.

The spatial distribution of molecular gas recovered by these maps is consistent with the integrated maps in Figure 1, with

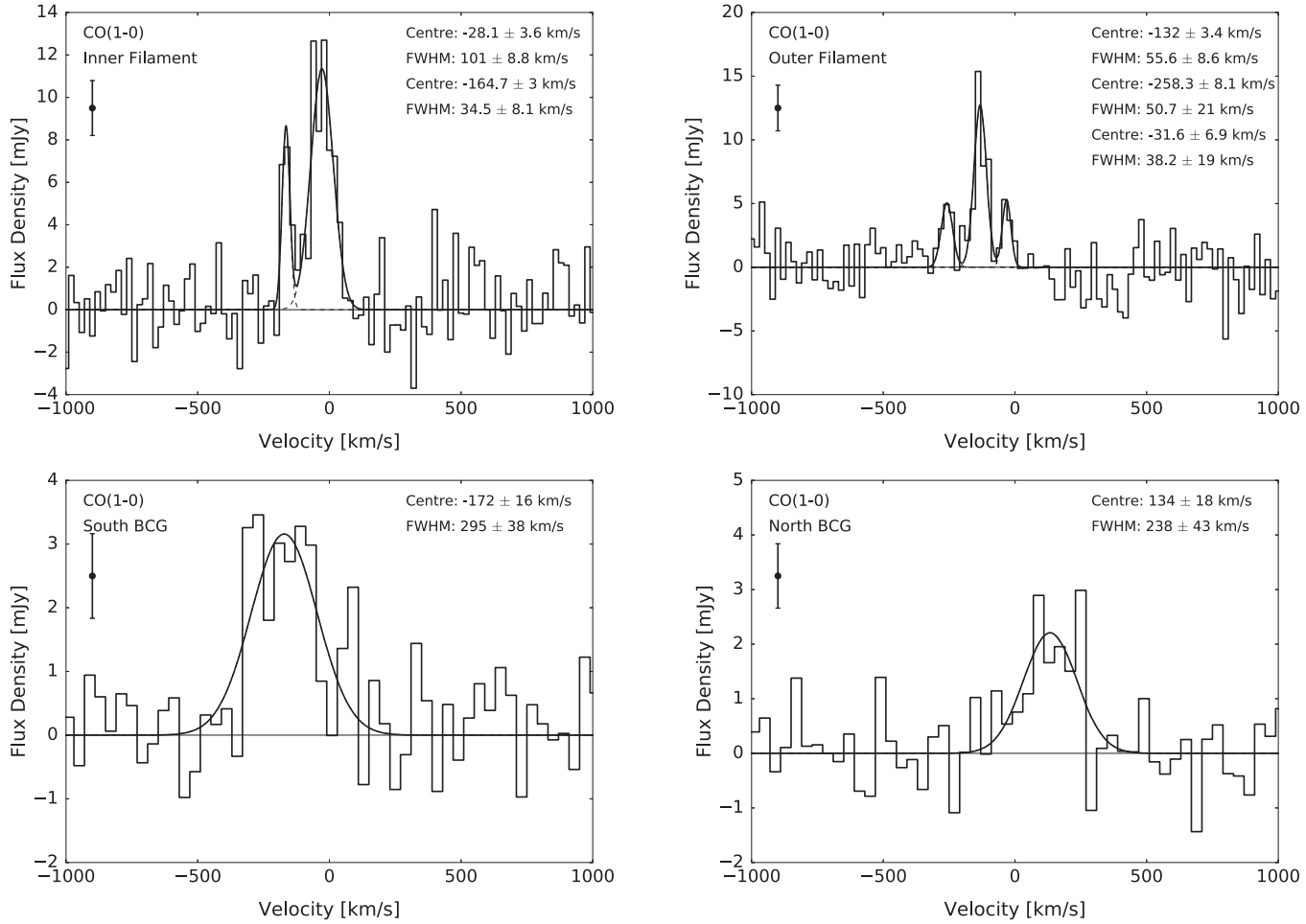

Figure 6. CO(1–0) spectra extracted from the regions shown in Figure 5. The best-fit parameters are given in Table 1. The error bar indicates the rms variation in the line-free channels. The "Inner Filament" and "Outer Filament" spectra are presented with 20 km s^{-1} velocity channels, while the "South BCG" and "North BCG" have been binned up to 40 km s^{-1} to improve the signal-to-noise ratio.

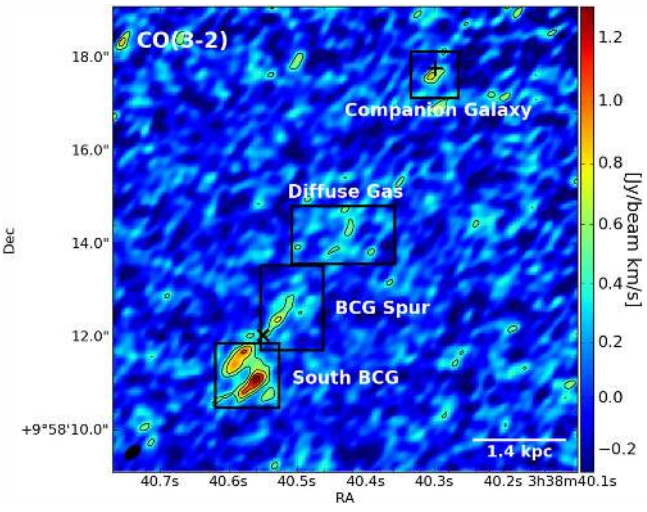

Figure 7. CO(3–2) integrated intensity map with regions highlighting the different structures seen in the BCG and the companion galaxy. The associated spectra are shown in Figure 8. The field of view is 10″ (7 kpc) on a side, showing the same area as in Figure 1.

the molecular gas divided between the BCG and a long filament north of the companion galaxy. Significant emission is detected along the entire length of the filament, confirming that the two clumps seen in Figure 1 are connected by a faint channel. The apparent disconnect between the inner and outer filament seen in Figure 1 arises because the maps were integrated over a velocity range much broader than the linewidth of this channel, drowning out the signal.

A large velocity gradient is present within the core of the BCG. South of the nucleus the gas is blueshifted to -210 ± 10 km s^{-1}, while the velocity of the spur extending to the north increases from 80 ± 10 km s^{-1} near the nucleus up to about 200 km s^{-1}. The blueshifted emission is relatively broad, with a FWHM of 260 ± 20 km s^{-1}, while the redshifted emission is considerably narrower, with a FWHM of 90–130 km s^{-1}. The smooth gradient observed between these regions results from the beam smearing together regions of disparate velocities. This velocity gradient is more pronounced at CO(3–2), where the velocity changes abruptly across the nucleus.

South of the BCG nucleus the two clumps identified at CO (3–2) share a broad velocity component (FWHM 200–300 km s^{-1}) with a shallow velocity gradient ranging from of -120 km s^{-1} in the southwest to -200 km s^{-1} in the northeast. A second velocity component is present in the southwestern clump, with a velocity of -270 km s^{-1} and FWHM of 80 km s^{-1}.

North of the BCG nucleus the CO(3–2) emission becomes more diffuse farther from the galactic center, with significant

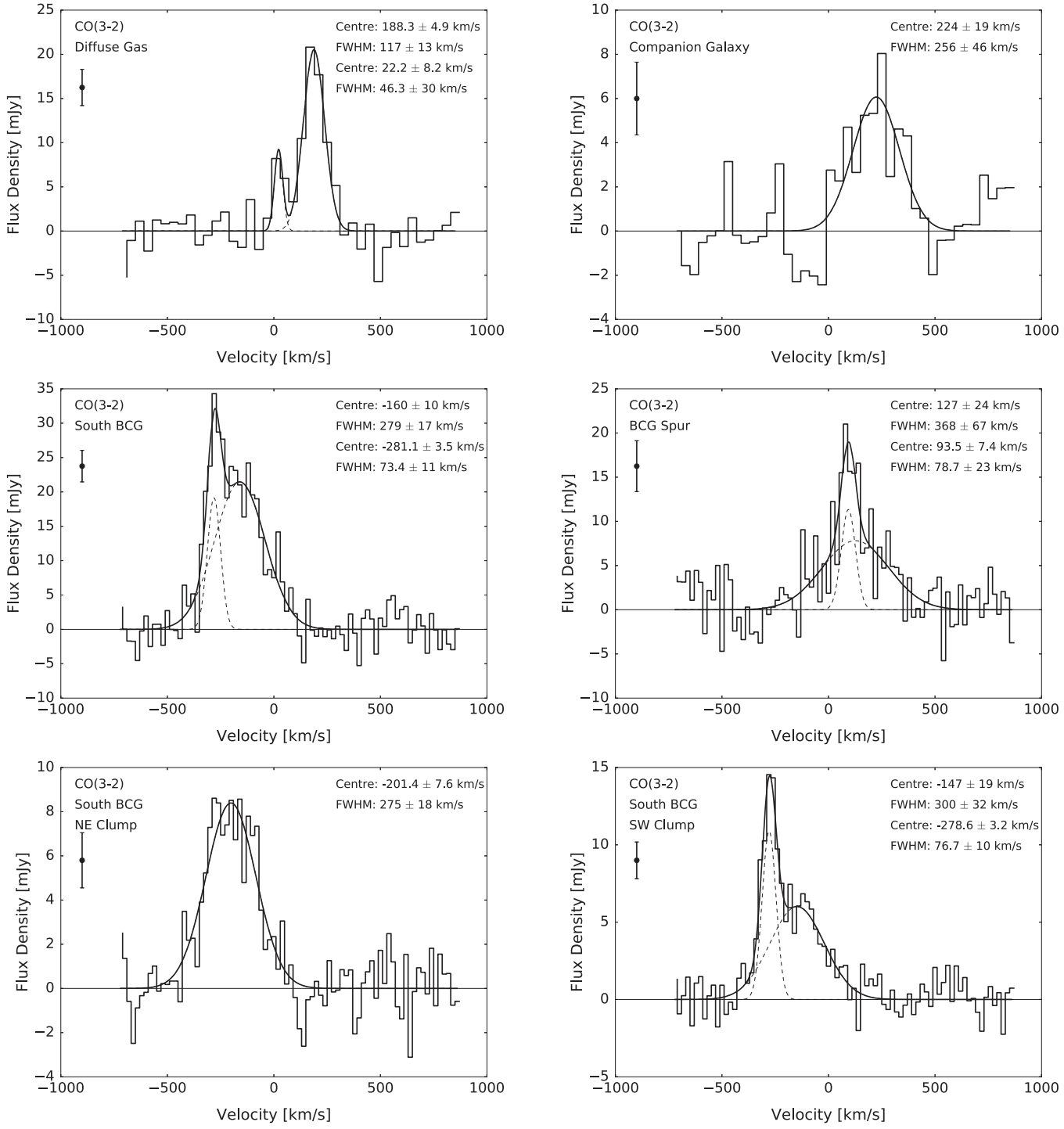

Figure 8. CO(3–2) spectra extracted from the regions shown in Figure 7. Additional spectra are shown for each of the two clumps within the South BCG region, which were extracted from $0\farcs6 \times 0\farcs6$ boxes. The best-fit parameters are given in Table 1. Each spectrum was initially extracted with 20 km s^{-1} velocity bins. The "Diffuse Gas" spectrum was binned up to 40 km s^{-1} channels to improve the signal-to-noise ratio, and "Companion Galaxy" was binned to 60 km s^{-1}. The error bar indicates the rms variation in the line-free channels.

detections obtained further from the nucleus than at CO(1–0). This emission follows the same gradient as the CO(1–0) emission, increasing from 80 km s^{-1} near the nucleus to 180–250 km s^{-1} in the diffuse clouds. A small region with higher velocity (170 km s^{-1}), broad (230 km s^{-1}) emission is observed immediately north of the nucleus, beside the 80 km s^{-1} emission. This map also reveals a significant detection coincident with the companion galaxy, which has a velocity of 240 km s^{-1} and a FWHM of 200–300 km s^{-1}.

Several distinct velocity structures are observed along the filament. Most of the emission originates from the "inner filament" (Figure 5), which occupies a very narrow range in velocity (-20 to -40 km s^{-1}) with a FWHM of only 70–100 km s^{-1}. Toward the tail of the filament the velocity becomes increasingly blueshifted to -145 km s^{-1}, where it then bends northward and the velocity further increases in magnitude to -230 km s^{-1}. Finally, a narrow tendril protrudes westward from the southern edge of the inner filament, with a

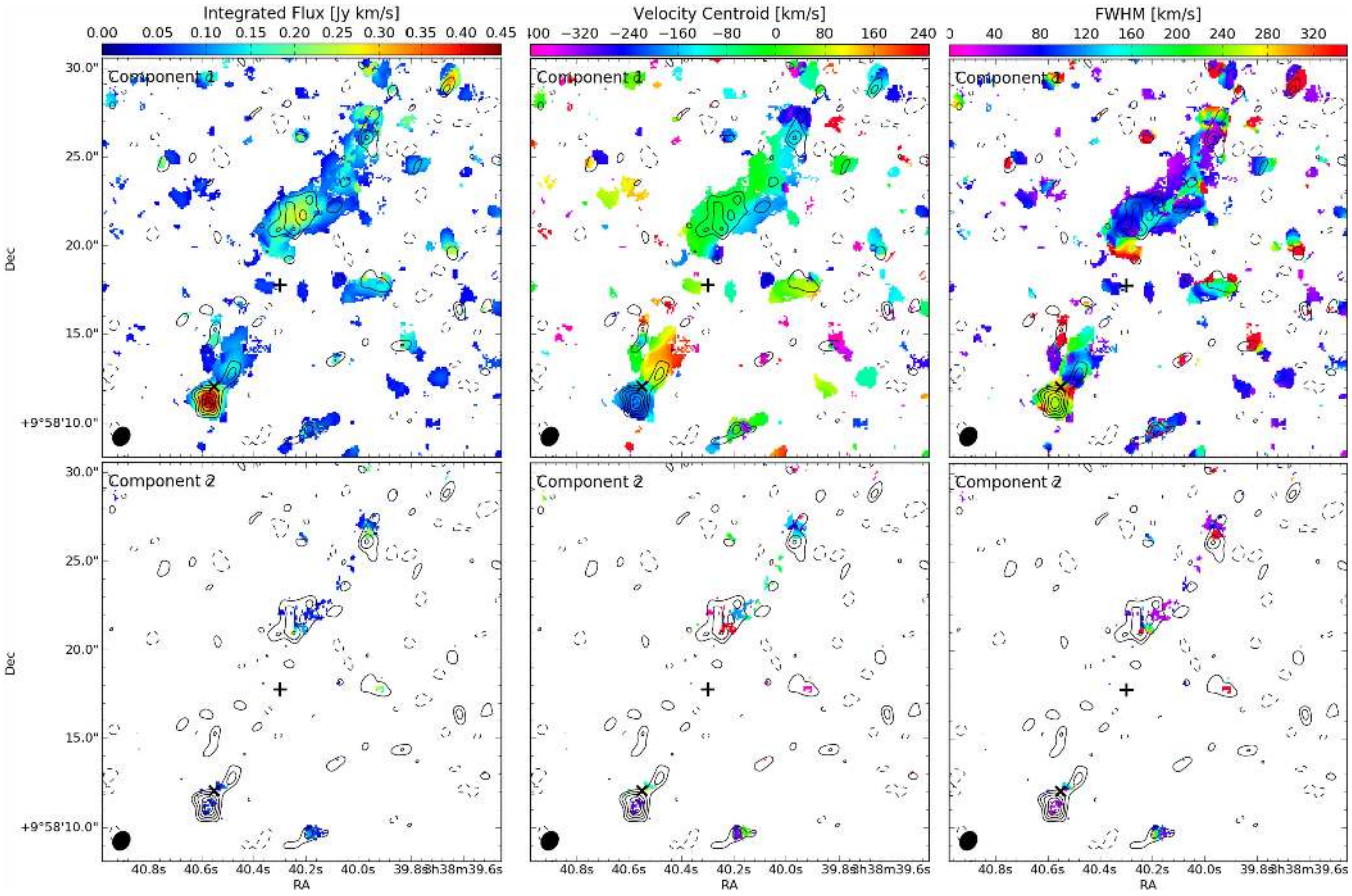

Figure 9. Maps of integrated flux (left), velocity centroid (middle), and FWHM (right) obtained from pixel-by-pixel fitting of the CO(1–0) datacube, as described in the text. Only pixels containing flux detected at $>2\sigma$ are shown. The contours are the same as in Figure 1 (top). The $\times$ and $+$ indicate the centroids of the BCG and companion galaxy, respectively.

velocity of -120 to $-170\,\mathrm{km\,s^{-1}}$ and a linewidth comparable to the inner filament. Multiple velocity components are detected at the interface between this tendril and the inner filament, extending all the way along the filament.

3.4. Velocity Profiles

Position–velocity (PV) diagrams of the molecular gas in both the BCG and the elongated filament are presented in Figure 11. For each PV diagram the flux was averaged over the width of the slit as a function of both slit position and velocity channel. One slit was placed along the extended axis of the molecular gas within the BCG, encompassing both the clump to the SE and spur to the NW. This slit was 1.″3 wide at CO(1–0) and 0.″84 wide at CO(3–2), both with a position angle (PA) of 147°. A second, 0.″52 wide slit was placed roughly orthogonal to this (PA 47°) in order to separate the two clumps identified at CO(3–2) but unresolved at CO(1–0). Finally, a 1.″5 wide slit (PA 130°) was placed lengthwise along the filament at CO (1–0). The position indicated in the PV diagrams runs from the bottom edge of the slits shown on the integrated flux maps to the top edge, with zero offset corresponding to the midpoint of the slit.

The PV diagrams along the long axis of the BCG (Figure 11 top) are qualitatively consistent between CO(1–0) and CO (3–2). The gas south of the nucleus is blueshifted and very broad. Extending toward the other side of the nucleus the velocity increases roughly linearly until the edge of the diffuse emission noted in CO(3–2) (see Figure 7). Gas coincident with the companion galaxy is also detected at CO(3–2), where the velocity is comparable to that of the diffuse emission.

The perpendicular cut across the nucleus in CO(3–2) shows the phase space information for the two clumps south of the BCG nucleus. The velocities of both clumps are $\sim -275\,\mathrm{km\,s^{-1}}$. The brighter clump is best fit by two velocity components in the velocity maps shown in Figure 6. The narrow component is also visible in the PV diagram, and appears to extend between the two clumps. The similar velocities in these structures indicate that the clumps are likely related dynamically.

All of the emission along the extended filament is confined to the range of -200 to $0\,\mathrm{km\,s^{-1}}$. However, the gas appears to be separated into two clumps. Higher blueshifted velocities are observed toward the tail of the filament, with velocities closer to systemic appearing at its base. The velocity of the inner portion of the filament is relatively constant along its entire 4″ (3 kpc) length. An infall model has been overlaid on this PV diagram (see Section 4.3.2).

3.5. Spatial Correlation with Dust Extinction

Two regions of significant extinction were noted by Donahue et al. (2007) in the archival *HST* WFPC2 F606W image of 2A 0335+096. A wedge-shaped region is located southwest of the BCG nucleus, and an elongated filament extends north of the companion galaxy as seen in Figure 1.

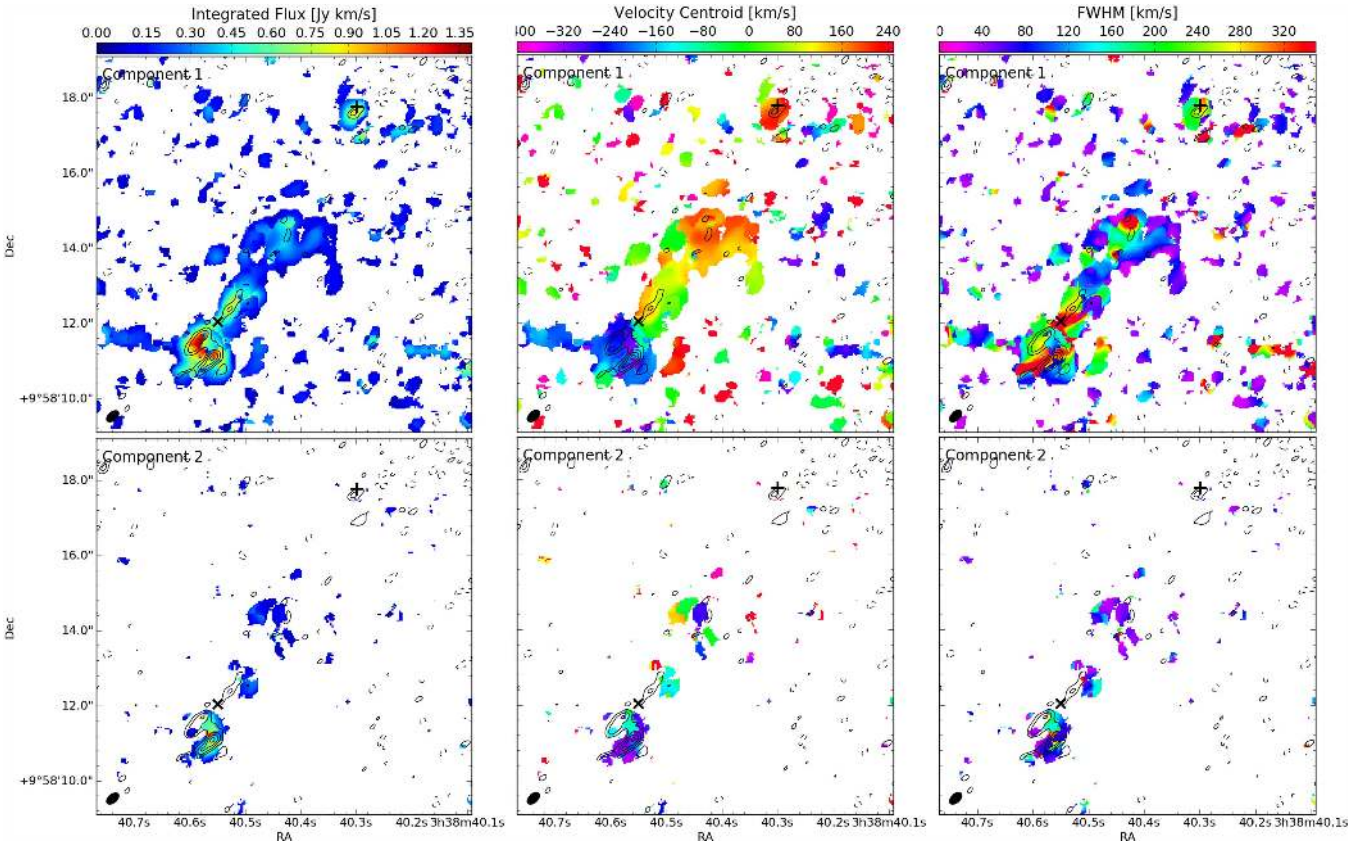

Figure 10. Maps of integrated flux (left), velocity centroid (middle), and FWHM (right) of a two-component fit to the CO(3–2) emission line. Only pixels containing flux detected at $>2\sigma$ are shown. The contours are the same as in Figure 1 (bottom). The $\times$ and $+$ indicate the centroids of the BCG and companion galaxy, respectively.

Both of these regions are coincident with significant amounts of molecular gas.

The calibrated *HST* WFPC2 F606W image was obtained from the Hubble Legacy Archive. All magnitudes quoted here have been transformed to the Johnson V-band using $m_V\,(\mathrm{Vega}) - m_{\mathrm{F606W}}\,(\mathrm{ST}) = 0.04$ derived for the Kinney et al. (1996) elliptical galaxy template in the IRAF tool Synphot. The $V - I$ color of the template galaxy, 1.3, is similar to that of a BCG, 1.2, so this conversion should be appropriate (Whiley et al. 2008). The quoted magnitudes have also been corrected for foreground Galactic extinction (A_{F606W}), K-correction, evolution of the stellar population, and surface brightness dimming. The applied corrections are shown in Table 2.

In order to quantify the dust extinction we model the two-dimensional (2D) distribution of stellar light using the galaxy-fitting code Galfit-M (Häußler et al. 2013), an extended version of Galfit (Peng et al. 2002, 2010). A Sérsic profile significantly overestimates the flux in the core of the BCG, an effect that is common in BCGs (Lauer et al. 2007; McNamara et al. 2009) and is thought to be caused by black hole scouring (Kormendy et al. 2009). The BCG is better modeled by the core-Sérsic profile (Graham et al. 2003), which is a Sérsic profile that transitions to a power law below the break radius r_b and is given by

$$I = I'\left[1 + \left(\frac{r_b}{r}\right)^{\alpha}\right]^{\gamma/\alpha} \exp\left[-\kappa\left(\frac{r^{\alpha} + r_b^{\alpha}}{r_e^{\alpha}}\right)^{1/(\alpha n)}\right]. \quad (2)$$

Here r_e and n are the effective radius and Sérsic index defined in the typical Sérsic profile, and the coefficient κ is a function of n. The transition and inner power law are described by the indices α and γ, respectively. The companion galaxy is modeled using a normal Sérsic profile and fit simultaneously with the BCG.

Structures unrelated to the BCG and companion galaxies' stellar light were masked out prior to fitting. These included background galaxies, a bright foreground star in the SE, and the obvious dust features in the filament and the BCG nucleus. A wide detector artefact at the edge of the CCD was also masked out, and limits the fittable area considerably. The resulting fit parameters are shown in Table 3. The companion galaxy is well modeled by a Sérsic profile with index 1.8 and total V-band magnitude 16.8. Using the same photometric corrections as the BCG, its absolute magnitude of -19.1 is slightly brighter than a dwarf galaxy.

Several biases are present in this fitting procedure. First, the fittable area is small due to the foreground star and a large detector artefact near the edge of the CCD. Since 2A 0335 +096 is a nearby cluster, these fits do not extend far into the envelope of the galaxy. The full shape of the BCG's light profile cannot be traced, so its effective radius is unconstrained. This also results in a large Sérsic index, since a power law provides a sufficient fit beyond the core. Second, the light profiles of galaxies are best fit when their position angle and ellipticity are allowed to vary as a function of radius. Isophotal variations are not currently supported by Galfit-M. Using the

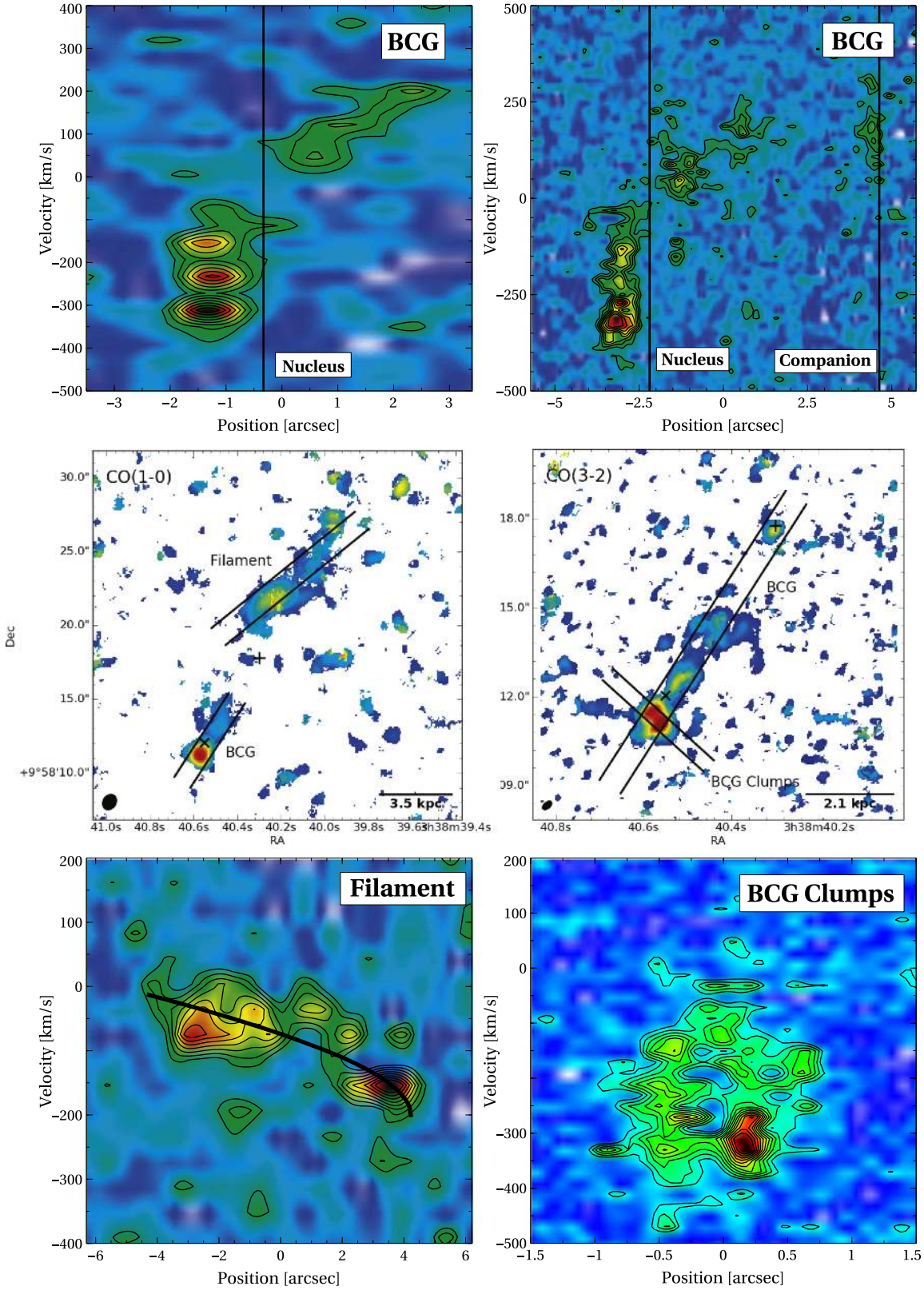

Figure 11. CO(1–0) (left) and CO(3–2) (right) position–velocity (PV) diagrams along the BCG (top), elongated filament (bottom left), and a perpendicular cut across the BCG (bottom right). In all cases the eastern (left) end of the slit corresponds to a negative position. The middle row shows the location of the slits overlaid on the integrated fluxes determined from the velocity maps of Figures 9 and 10. The vertical lines in the PV diagrams indicate the locations of the BCG nucleus and companion galaxy. The PV diagram of the extended filament in CO(1–0) (bottom left) is overlaid with a gravitational free-fall model, as discussed in Section 4.3.2.

Table 2
Photometric Corrections

Galactic Extinction[a] (mag)	K[b] (mag)	Evolution[b] (mag)	$(1+z)^4$ (mag)
0.989	0.073	−0.047	0.148

Notes.
[a] Schlafly & Finkbeiner (2011).
[b] Poggianti (1997).

Table 3
2D Optical Fitting Results

	Units	BCG	Companion
$I(r_b)$[a]	mag arcsec^{-2}	19.310 ± 0.005	…
r_b	arcsec	0.924 ± 0.007	…
α		2.56 ± 0.05	…
γ		0.081 ± 0.004	…
$m_{\rm tot}$	mag	…	16.736 ± 0.003
r_e	arcsec	Unconstrained[b]	0.997 ± 0.002
$\frac{d\ln I}{d\ln r}$		−1.35[c]	…
n		19.6 ± 2.8	1.838 ± 0.005
b/a		0.7010 ± 0.0004	0.884 ± 0.001
PA	degrees	−21.85 ± 0.06	7.8 ± 0.5

Notes.
[a] $I(r_b)$ is related to I' in Equation (2) via $I' = I(r_b)\ 2^{-\gamma/\alpha}\ \exp[\kappa\ (2^{1/\alpha}\ r_b/r_e)^{1/n}]$.
[b] The BCG radii probed by the *HST* imaging only show a bend at the break radius. The Sérsic component is close to a power law, with the corresponding effective radius lying outside of the *HST* field of view.
[c] Since the effective radius is unconstrained, we quote the logarithmic derivative at a radius of 20″ instead.

ELLIPSE task in IRAF to extract elliptical isophotes of the stellar light favors a position angle of −5° to −10° in the center, twisting to −30° beyond 10″. Similarly, the axis ratio b/a is consistent at large radii with the 0.7 measured here, but decreases to 0.65 in the core.

In Figure 12 we present a map of the dust extinction, showing the ratio of image surface brightness to the model brightness (I/I_0). Regions with significant extinction are highlighted by the labelled ellipses, with the corresponding extinction (both the peak extinction in a pixel and mean within the ellipse) tabulated in Table 4. These regions were confirmed by eye in the original image. Systematic errors are clearly visible in the residuals of the extinction map, primarily perpendicular to the BCG–companion axis. Positive and negative residuals near the BCG centroid (red ×) correspond to a double-peaked nucleus, so the extinction northwest of region *A* does not correspond to dust. The extinction surrounding the labelled dust features is generally $\lesssim$5%, though increases to ∼10% around the filament. Model residuals surrounding the identified regions also typically have $I/I_0 \geqslant 1$, so the tabulated optical depths and dust masses may be underestimated.

The mean optical depth τ is computed from the mean extinction via $I/I_0 = e^{-\tau}$. This is converted into column density (N_H), assuming a standard V-band Galactic extinction curve (Cardelli et al. 1989), through $N_H = 2.05 \times 10^{21}\ \tau_V\,{\rm cm}^2$ and finally to dust mass. Region *A* is coincident with a clump of molecular gas identified at CO(3–2). Taking CO(3–2)/CO(1–0) = 7, the corresponding molecular gas mass is $9.5 \times 10^7\ M_\odot$ and gas-to-dust ratio is 130, which is similar to the Milky Way value. Regions *F* through *I* are coincident with the extended filament. The total dust mass in these regions is $1.07 \pm 0.07 \times 10^7\ M_\odot$. With a molecular gas mass of $7.8 \pm 0.9 \times 10^8\ M_\odot$, the local gas-to-dust ratio is 66. This is a factor of two lower than the gas-to-dust ratio in the BCG. Regions *B* and *D* are coincident with molecular gas in the northern spur and companion galaxy, respectively, although neither traces the gas distribution well. Attributing all of the molecular gas in the spur to region *B* results in a gas-to-dust ratio of 290, although the differing spatial distributions add considerable uncertainty to this value.

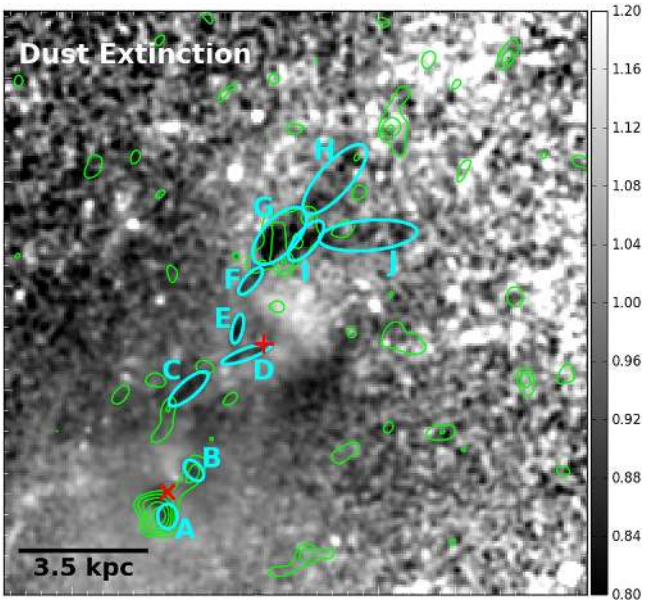

Figure 12. Dust extinction map of the *HST* F606W image. Regions with significant dust extinction are identified by the green ellipses, with statistics shown in Table 4. The BCG and companion galaxy centroids are identified by the red× and +, respectively. The image is shown in the same field of view as the ALMA CO(1–0) image (Figures 1 and 9). The CO(1–0) contours from Figure 1 have been overlaid for reference.

Treating the dust as a thin screen, for regions G–J, where the minima of I/I_0 are about 0.5, the dust must lie on or in front of the midplane of the BCG. The velocity of the molecular gas in these regions is within a few tens of km s^{-1} from the systemic value, and the FWHM is 100 km s^{-1} at its broadest. Taken together, these suggest that the filament is oriented roughly perpendicular to the line of sight, possibly flowing on a nearly radial trajectory toward the BCG. The lesser peak extinction within the BCG, where the minimum of $I/I_0 \simeq 0.82$, means that the location of the dust along our line of sight is poorly constrained.

Overall the most significant associations of molecular gas are coincident with significant dust extinction. Dust shielding in these regions may be promoting the formation of molecular gas. It is also possible that the more extended associations (such as along the spur) do not have detected dust extinction because the dust has been spread out over a larger area, resulting in too low a column density for visible dust extinction.

3.6. Spatial Correlation with X-Ray and Hα Filaments

2A 0335+096 hosts a bright Hα nebula with total luminosity $L_{\rm H\alpha} = 0.8 \times 10^{42}$ erg s^{-1} (Donahue et al. 2007).

Table 4
Dust Extinction

Region	Area (10^{42} cm^2)	$(I/I_0)_{\rm min}$	I/I_0	$\langle\tau\rangle$	N_H (10^{20} cm^{-2})	$M_{\rm dust}$ ($10^5\,M_\odot$)
A	2.58	0.82 ± 0.03	0.923 ± 0.005	0.080 ± 0.005	3.42 ± 0.23	7.4 ± 0.5
B	2.0	0.88 ± 0.04	0.938 ± 0.006	0.064 ± 0.006	2.75 ± 0.27	4.6 ± 0.5
C	4.52	0.80 ± 0.06	0.896 ± 0.007	0.110 ± 0.007	4.69 ± 0.32	17.7 ± 1.2
D	3.12	0.81 ± 0.02	0.944 ± 0.005	0.057 ± 0.005	2.45 ± 0.23	6.4 ± 0.6
E	1.58	0.72 ± 0.05	0.884 ± 0.010	0.123 ± 0.012	5.25 ± 0.50	6.9 ± 0.7
F	2.3	0.76 ± 0.09	0.922 ± 0.014	0.081 ± 0.015	3.46 ± 0.63	6.7 ± 1.2
G	13	0.48 ± 0.08	0.884 ± 0.007	0.123 ± 0.008	5.26 ± 0.35	57.0 ± 3.8
H	14.9	0.56 ± 0.10	0.962 ± 0.009	0.039 ± 0.009	1.66 ± 0.39	20.7 ± 4.8
I	5.24	0.56 ± 0.09	0.886 ± 0.012	0.121 ± 0.013	5.16 ± 0.23	22.6 ± 2.5
J	15.6	0.51 ± 0.10	0.959 ± 0.008	0.042 ± 0.009	1.79 ± 0.36	23.3 ± 4.7
Total						173 ± 8

While the Hα nebula is not associated with any structures in the 0.5–7 keV *Chandra* X-ray image, multi-temperature fits reveal a 0.5 keV component in the ICM that is spatially coincident with the Hα emission (Sanders et al. 2009). Similar spatial correlations have been observed in several other cool core clusters, including Perseus (Fabian et al. 2003, 2008), M87 (Sparks et al. 2004; Werner et al. 2013), and several nearby giant ellipticals (Werner et al. 2014). Filaments of molecular gas have been detected along the Hα filaments in Perseus (Salomé et al. 2006, 2008; Lim et al. 2008, 2012), implying that the co-spatial gas in the filaments occupies 5–6 decades in temperature.

Multiphase gas spanning many decades in temperature is also observed here. Figure 13 shows the Hα nebula from Donahue et al. (2007) overlaid with contours of the CO(1–0) emission. The two distributions are qualitatively very similar. Bright Hα emission near the BCG extends in a spur toward the companion galaxy. The emission extends beyond the companion galaxy into a filament coincident with the extended filament of molecular gas seen in CO(1–0) emission. However, the most luminous nebular emission is in the BCG, while the molecular gas is observed preferentially in the filaments. This may be due to line emission that has been resolved out by the interferometer. Only 40% of the single dish flux has been recovered here, so a diffuse component of cold gas may be present in the BCG.

Integral field spectroscopy of the Hα nebula reveals that the [N II] λ6583 line and the molecular gas are co-located in both position and velocity space (Farage et al. 2012). Broad, blueshifted emission is slightly offset to the south of the BCG with a velocity of about $-120\,{\rm km\,s^{-1}}$ ($-240\,{\rm km\,s^{-1}}$ in our adopted frame). Near the companion galaxy the Hα nebula becomes redshifted with respect to the systemic velocity, with blueshifted emission extending along the direction of the filament. Farage et al. (2012) also detected nebular emission 5–10 kpc southeast of the BCG nucleus. Its redshifted velocity led them to conclude that the nebula is in rotation about the center of the BCG with a velocity amplitude of $130\,{\rm km\,s^{-1}}$. Molecular gas either does not extend along the southeastern arm of the filament or is too faint to detect, so we are unable to corroborate this finding. The lack of molecular gas to the southeast may arise if the surrounding atmosphere lacks the dense regions required to form H_2, or if H_2 production is enhanced by the presence of dust grains to the northwest. Since our observations trace only the high-density molecular gas (see Section 3.2), molecular gas may lie to the southeast but falls below our detection limit.

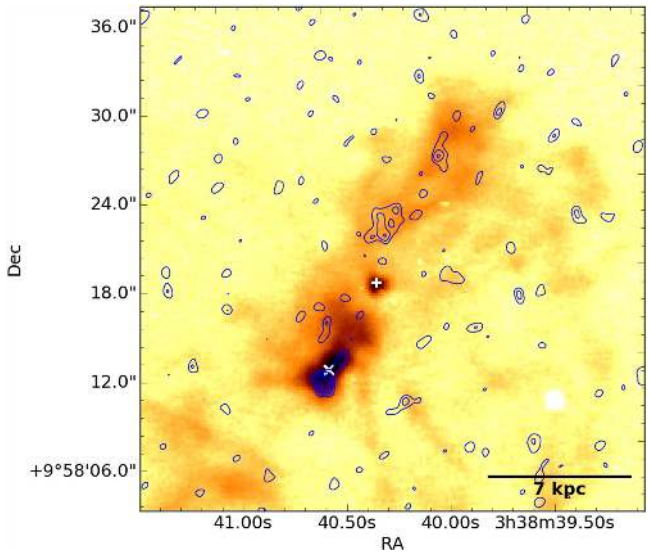

Figure 13. Hα emission from Donahue (2007) overlaid with the CO(1–0) contours from Figure 1. The $\times$ and $+$ indicate the nuclei of the BCG and companion galaxy, respectively. The coordinate reconstruction of the Hα image is accurate to $\sim 1''$.

4. DISCUSSION

4.1. Origin of the Molecular Gas

With a total molecular gas mass exceeding $10^9\,M_\odot$, 2A 0335 +096 harbours significantly more molecular gas than is typically observed in early-type galaxies. Identifying the origin of this gas is critical in understanding the evolution of the BCG. Two primary mechanisms could be contributing to this gas: stripping of merging galaxies or cooling from the hot atmosphere.

Large supplies of molecular gas are observed preferentially in BCGs at the centers of galaxy clusters with cooling times falling below 1 Gyr. These systems are associated with bright emission-line nebulae and enhanced star formation. Thus the presence of molecular gas should in general be linked to residual cooling of the hot atmosphere.

The presence of a companion galaxy located 5 kpc from the BCG in projection raises the possibility of a merger origin for the molecular gas in this system. Its low stellar velocity

(~200 km s^{-1}; Gelderman 1996) relative to the BCG suggests that the galaxies also have a small radial separation. The trail of molecular gas orientated toward the companion galaxy may then be indicative of an interaction between the two galaxies.

Before delving further into the origin of the molecular gas, we emphasize the difference in dynamics between the two components. The inner edge of the filament is slightly blueshifted with respect to the stellar component of the BCG, while all nuclear gas north of the BCG is redshifted. Since the components are not smoothly connected in phase space, we treat them separately in our discussion.

Mergers with donor galaxies can supply gas to the BCG through several distinct avenues. Repeated mergers between the BCG and gas-rich donor galaxies are unlikely given the low number of member galaxies in this low-richness cluster (Schwartz et al. 1980), and because the high-velocity dispersion of a cluster decreases the merger rate. We instead focus only on a merger with the nearby companion galaxy. A tidal interaction between the galaxies may result in either the stripping of cold gas from the companion or the disruption of a pre-existing gas supply within the BCG. Alternatively, ram pressure stripping would form a tail that may correspond to the filament.

4.1.1. Tidal Interaction

In the nucleus of the BCG, the opposed redshifted and blueshifted velocities are suggestive of rotation. This velocity pattern is consistent with the H_2 kinematics derived from *K*-band integral field spectroscopy (Wilman et al. 2011) as well as lower-resolution Hα integral field spectroscopy of the nuclear barred structure (Hatch et al. 2007; Farage et al. 2012). The peak-to-peak velocity difference observed in CO(1–0) is ~400 km s^{-1} over a spatial scale of about 2 kpc. This is expected of molecular gas in merger remnants, which generally exhibits large-scale rotation with high velocities (Ueda et al. 2014).

Although ordered motion seems plausible at CO(1–0), the higher-resolution CO(3–2) maps show a highly asymmetric distribution of cold gas that is inconsistent with being a rotationally supported disk. Twice as much molecular gas is located south of the nucleus versus the north side, and the gas velocity jumps abruptly across the nucleus. This asymmetry indicates that any ordered structure must be in the process of forming, as the gas is not in an equilibrium structure. If the gas is orbiting the BCG, then it will form one complete spiral when the gas on the innermost orbit has circled the galaxy one more time than the gas on the outermost orbit. With resolved scales of 1–2 kpc and velocities of ~200 km s^{-1}, the corresponding disk formation timescale is $\sim 3 \times 10^7$ years. Since no disk-like structure is observed, the gas is either moving mainly in the plane of the sky or we are observing the system very recently after the stripping began.

Gas clumps oriented toward the companion galaxy have velocities that increase roughly linearly with projected radius to values matching the stellar velocity of the companion galaxy. An interaction between the companion galaxy and the BCG can account for the molecular gas via two scenarios: either the gas is tidally stripped from the companion, or the passage of the companion through a pre-existing gas supply has dredged up the gas. Differentiating between the original source of the molecular gas is difficult with the current data. Given the greater recession velocity of the companion, if it has already interacted with the BCG, it is now receding from the BCG, moving outward in projected radius and away behind the midplane of the BCG.

In the first scenario, direct stripping from the companion would initially maintain the sign of the velocity, with the magnitude decreasing as the gas is slowed by the gravity of the BCG. At later times the gas will reverse direction and fall back onto the BCG. The persistent redshifted velocities observed here then imply that the interaction was recent, as the clouds have not yet reversed in direction. If even half of the gas distributed between the galaxies originated in the companion, then its molecular gas mass would have initially been $\sim 1.2 \times 10^8\, M_\odot$, double its current mass. This is relatively gas-rich compared to the ellipticals in Virgo (e.g., Young et al. 2011). A merger with a gas-rich donor galaxy is certainly possible, but is unlikely to be expected a priori.

Following the second scenario, gas originating in the BCG that is pulled outward by the companion would have a velocity that increases with radius as it is accelerated away from the BCG, as observed. When the companion is far enough away, the BCG will again dominate the potential and any gas that is not bound to the companion will rain back onto the BCG. The 1.5 kpc gap between the companion and the farthest extent in the spur suggests that this has occurred recently and the clumps between galaxies may now be dominated once again by the BCG. Although no stellar dispersion is available for the companion, the linewidth of its molecular gas (260 km s^{-1}) is typical of a normal galaxy, suggesting that the molecular gas has had time to settle into its gravitational potential well. From the "BCG" spectrum presented in Figure 3, the masses of the redshifted and blueshifted peaks are consistent, containing $1.5 \pm 0.3 \times 10^8\, M_\odot$ and $1.7 \pm 0.3 \times 10^8\, M_\odot$, respectively. If these originated from the same reservoir, then the tidal disruption would have removed ~50% of the pre-existing gas supply.

With a projected separation of 4.5 kpc, an interaction between these galaxies would have occurred roughly 20 Myr ago, assuming the line-of-sight speed of the companion is representative of its 3D velocity. However, if the velocity is this low near the cluster core, then the companion cannot be on its first passage through the cluster, as several orbits would be required to decelerate the galaxy. If the companion is on its first passage then it must be travelling near the plane of the sky. Its transverse velocity would be several times greater than its line-of-sight velocity, decreasing the interaction time by a factor of a few.

Importantly, tidal interactions affect all matter within the galaxy, without regard to its phase. Stars should therefore be affected just as strongly as the molecular gas. This is not observed in the *HST* imaging, as the stellar light does not show strong deviations from a smooth profile. Removing half of a pre-existing gas reservoir via tidal forces is therefore unlikely. It is possible that an interaction between these galaxies has not yet begun, potentially from a radial offset between them, but the similarity in velocity between the companion and the series of clumps appears too striking to be a coincidence.

We again emphasize that the tidal stripping discussed here only attempts to account for the molecular gas within the BCG; the filament must be formed separately. The molecular filament cannot have originated from an older merger, as the merger rate is low and the gas would have already fallen onto the BCG. Instead we must invoke a separate mechanism entirely, such as

cooling from the hot atmosphere. It is far more likely that the molecular gas is produced via one primary mechanism, and that the companion galaxy has merely disrupted a pre-existing gas supply.

4.1.2. Ram Pressure Stripping

In the dense cores of galaxy clusters, the ram pressure exerted on atomic gas in an infalling galaxy is enough to overcome its gravitational binding energy, allowing the gas to be efficiently stripped from its host galaxy (Haynes et al. 1984; di Serego Alighieri et al. 2007; Grossi et al. 2009). Molecular gas is more difficult to strip than atomic gas because molecular clouds have a much smaller surface area than atomic nebulae and they reside deeper within the galaxy's gravitational potential. Galaxies in the Virgo cluster with strong HI deficiencies have minimal molecular gas deficiencies (Kenney & Young 1989), and the CO detection rate in the cluster is the same as in the field (Young et al. 2011). However, ram pressure stripping of molecular gas has still been observed in the Virgo (e.g., Vollmer et al. 2008), Norma (Jáchym et al. 2014), and Coma clusters (P. Jáchym et al. 2016, in preparation). If the companion galaxy is indeed falling into the cluster, then ram pressure stripping might be a viable source of the $7.8 \times 10^8\,M_\odot$ of molecular gas in the filament. This, however, is not a viable mechanism for supplying the large reservoirs of molecular gas in BCGs in general, since molecular gas is observed preferentially in BCGs residing at the centers of clusters with short central cooling times.

The Norma cluster galaxy ESO 137-001 is the first system found to contain a large amount of molecular gas in a ram pressure stripped tail, with a total molecular gas mass exceeding $10^9 M_\odot$ (Jáchym et al. 2014). This molecular gas is associated with a 40 kpc long tail of Hα emission and an 80 kpc long X-ray tail, with a total HI upper limit of $\sim 2 \times 10^9\,M_\odot$. The presence of soft X-ray emission in the tail is expected to arise from the mixing of the cold, stripped interstellar medium with the hot intracluster gas (Sun et al. 2006; Tonnesen et al. 2011). Jáchym et al. (2014) suggest that the molecular gas in the outer extent of the tail has formed in situ out of stripped atomic gas, while the inner reaches of the tail may also be comprised of molecular clouds that were stripped directly from the infalling galaxy.

The spatial correlation of molecular gas with Hα and X-ray emission in ESO 137-001 resembles the filament trailing the companion galaxy in 2A 0335+096. Evidently, ram pressure stripping of gas from a high velocity infalling galaxy is able to form a filament similar to that observed in 2A 0335+096. This offers a natural explanation for the significant dust extinction observed along the filament, which would be stripped from the companion galaxy along with the atomic and molecular gas, and would offer a seeding site for in situ molecular gas formation. Since the line-of-sight speed of the molecular gas along the filament is $\lesssim 200\,\mathrm{km\,s^{-1}}$, the high infall velocity required to form the filament via ram pressure stripping would require that most of the motion be along the plane of the sky.

Ram pressure stripping requires a very high relative velocity in order to form the observed filament. Orbit modeling in ESO 137-001 favors infall velocities of $\gtrsim 3000\,\mathrm{km\,s^{-1}}$. The necessary relative velocity in 2A 0335+096 is not this severe, since the companion galaxy is situated closer to its cluster center so is in a higher-density environment, lessening the demands on velocity. Extrapolating the Sanders et al. (2009) gas density profile assuming a power law of $n_e \propto r^{-1}$, the ICM density at the base of the filament ($\sim$13 kpc) is $\approx 0.07\,\mathrm{cm^{-3}}$. This is 35 times greater than the ICM density at the location of ESO 137-001, using the β-model parameters in Table 7 of Jáchym et al. (2014). Assuming that the force exerted by ram pressure, ρv^2, is the same here as it is in ESO 137-001, the infall velocity required to produce the tail is $\sim 500\,\mathrm{km\,s^{-1}}$. Since the line-of-sight velocity of the companion galaxy is $230\,\mathrm{km\,s^{-1}}$, the inclination of the filament would need to be about 30°.

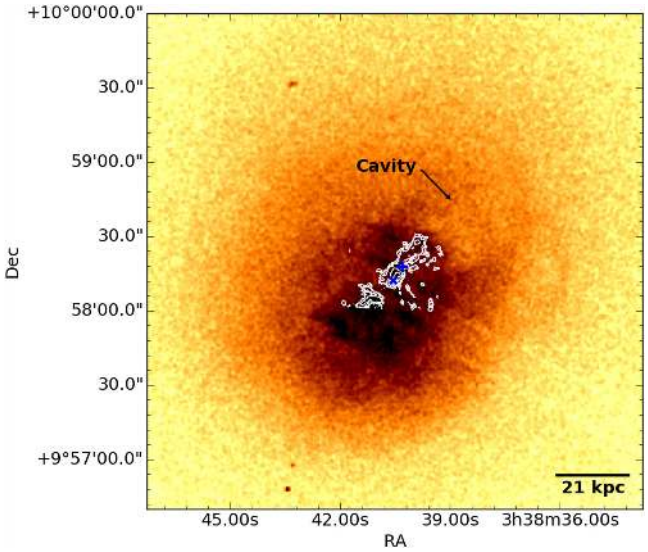

Figure 14. *Chandra* X-ray image of the hot atmosphere of 2A 0335+096. Several X-ray cavities and clumps of cool gas are visible in the image. The Hα nebula, shown in white contours, extends toward the most energetic cavity. Any emission to the south of the contours has been masked out due to contamination by a foreground star.

As discussed in Section 4.1.1, the series of redshifted clumps located between the BCG and the companion suggests that the two galaxies have already interacted. If this is the case, then the companion galaxy must have passed through the BCG on a northwestward trajectory. This scenario is mutually exclusive with the ram pressure stripping origin of the filament, which requires that the companion be on its first passage through the cluster and travelling to the southeast.

Additionally, the morphology of the filamentary emission differs from what is expected from ram pressure stripping. First, the orientation of the filament does not coincide with the companion galaxy. Extending the inner edge of the filament to the southeast, the shortest distance between the filament and the companion is 2 kpc. Ram pressure stripping should form a tail in a direction directly opposing the direction of motion, which is not the case here. Second, Hα emission and soft X-rays are not confined to the region trailing the companion. Significant Hα emission is observed on both sides of the BCG, with the brightest emission surrounding the molecular gas within the BCG. This emission is visible in the lower left corner of Figure 13 as well as the contours of Figure 14, but its full extent is obscured due to the presence of a bright foreground star. If the filament is formed by ram pressure stripping then the Hα emission should be localized to the tail of the companion galaxy, in addition to whatever emission is associated with the molecular gas in the BCG.

4.1.3. Cooling of the Hot Atmosphere

Cooling from the hot atmosphere naturally explains the spatial correlation of gas over 5–6 decades in temperature. The upper limit on the mass deposition rate of the 0.5 keV X-ray emitting gas is $30\,M_{\odot}\,\mathrm{yr}^{-1}$ (Sanders et al. 2009), which can form the $7.8\times10^{8}\,M_{\odot}$ of molecular gas in the filament in 24 Myr or the entire gas reservoir in 40 Myr. Depletion of the molecular gas via star formation proceeding at a rate of $2M_{\odot}\,\mathrm{yr}^{-1}$ (O'Dea et al. 2008) increases the accumulation time by <10%. We also note that the cooling gas is distributed on larger scales than the molecular gas. Roughly half of the 0.5 keV gas is located on the side of the BCG opposite the molecular gas. This increases the accumulation time by roughly a factor of two, resulting in a total time of 50–90 Myr. This is approaching the mean outburst interval between generations of AGN outbursts of 10^{8} years (e.g., Vantyghem et al. 2014).

Most of the baryonic content in clusters is contained in the hot atmosphere, offering a vast reservoir which can supply the molecular gas. Approximating the central hot gas density profile in Sanders et al. (2009) with $\rho\propto r^{-1}$, the extrapolated gas mass within 13 kpc, which encloses all of the molecular gas, is $7.9\times10^{9}\,M_{\odot}$. This is about 7 times more than is needed to form the entire $1.13\times10^{9}\,M_{\odot}$ of molecular gas. However, cooling does not occur over the full azimuth, and the local supply of hot gas is much more restrictive. On the other hand, gas cooling out of the hot atmosphere can be replenished by gas from higher altitudes, providing more than the $7.9\times10^{9}\,M_{\odot}$ of gas within the central 13 kpc.

The presence of multiple cavities in the hot atmosphere (Mazzotta et al. 2003; Sanders et al. 2009) indicates that 2A 0335+096 has undergone several cycles of AGN feedback, which would include multiple cycles of cooling. However, if cooling has persisted over multiple cycles then we should expect to see several filaments, similar to those in Perseus (Hatch et al. 2006; Salomé et al. 2011), while only one is observed. Filaments from previous cooling cycles may have fallen back onto the BCG, forming the observed reservoir within it. Conversely, the presence of a single filament is reminiscent of the cooling wake observed in A1795 (Fabian et al. 2001; Crawford et al. 2005), where cooling is stimulated by the motion of the cD galaxy through the hot atmosphere. Sloshing motions in 2A 0335+096 indicate that the BCG is in motion with respect to the cluster, which may establish the preferred direction of cooling.

Gas cooling from the hot atmosphere is expected to be relatively dust-free (Donahue & Voit 1993). This is because dust grains are rapidly sputtered in the ICM, and can only form when the gas is shielded by UV and X-ray irradiation (Draine & Salpeter 1979). As noted in Section 3.5, significant dust extinction is present over much of the length of the filament. Since dust production from cooling gas is difficult, the dust likely originated from the within the BCG. Hatch et al. (2007) suggested that the dusty nebulae observed in several BCGs have been drawn out of the central molecular gas reservoir, where the high densities can provide shielding long enough for the gas to become polluted with dust.

Recent simulations have suggested that thermal instabilities in the hot atmosphere are induced along the direction of the radio jet (Gaspari et al. 2013; Li & Bryan 2014a), which is not the case in 2A 0335+096. A bipolar radio jet observed at 1.5 GHz extends 12 arcsec to the northeast and southwest of the BCG (Sarazin et al. 1995; Donahue et al. 2007), which is orthogonal to the filament. Instead, we argue in Section 4.2.1 that the preferred direction of gas cooling has been imposed by uplift from an X-ray cavity. This enables dust to be lifted out of the BCG, providing seeding sites for the production of molecular gas.

4.1.4. Summary: Gas Origin

While galaxy mergers are unable to account for the high molecular gas masses in cool core galaxy clusters in general, the presence of a close companion in this system has the potential to supply the cold gas. Tidal stripping from the companion galaxy can supply the BCG with cold gas, but does not account for the filament. Instead, the merger may have disrupted a pre-existing gas supply within the BCG, dredging up cold gas as it passed through. However, we do not see evidence for a tidal disruption in the stellar light of either galaxy. Alternatively, the filament observed in 2A 0335+096 resembles the ram pressure stripped tails in other systems (e.g., ESO 137-001). Ram pressure stripping is feasible if the companion is infalling from the northwest with a high relative velocity, and can account for the spatial coincidence of molecular gas, dust extinction, Hα emission, and soft X-rays. However, it does not explain the inclined orientation of the filament or the Hα emission and soft X-ray located southeast of the BCG nucleus. Furthermore, if gas has in fact been dredged up by the companion galaxy, then its implied orbit rules out the possibility of a ram pressure stripping origin of the filament. Cooling of the hot atmosphere provides a feasible mechanism for supplying the molecular gas that is tenable in a much broader sample of cool core clusters. The hot atmosphere harbours more than enough gas to produce the filament, and the 0.5 keV phase is cooling rapidly enough to form the entire molecular gas supply in $\sim10^{8}$ years. The cold gas within the BCG may then correspond to an older cycle of cooling from the hot atmosphere that has fallen onto the BCG.

4.2. Origin of the Cooling

4.2.1. Cooling Stimulated by the AGN

Following recent ALMA observations of PKS0745-191 (Russell et al. 2016) and A1835 (McNamara et al. 2014), McNamara et al. (2016) proposed the "stimulated feedback" model. In this model, molecular gas condenses from lower-entropy gas that is lifted outward from the cluster core by X-ray bubbles, away from the location where the heating rate matches its cooling rate. Unless the overdensity falls back to its original position within its cooling time, it will condense out of the ICM (Nulsen 1986; Revaz et al. 2008; Gaspari et al. 2013; Li & Bryan 2014b), forming molecular gas and emission-line nebulae.

The molecular gas in the PKS0745-191 BCG is distributed along three narrow filaments that are 3–5 kpc in length (Russell et al. 2016). Two of the filaments are oriented behind X-ray cavities, while the third is coincident with UV emission from young stars. The velocities of the cold gas, which lie within $\pm100\,\mathrm{km\,s}^{-1}$ of the systemic velocity, are too low to arise from steady inflow of clouds condensing out of the hot atmosphere. Instead, the velocity distribution of the two filaments oriented toward X-ray cavities are consistent with the majority of the gas flowing outward from the galaxy center.

A similar outflow was observed in the A1835 BCG, where $10^{10}\,M_{\odot}$ of cold gas is located in a bipolar flow behind two

X-ray cavities (McNamara et al. 2014). This system hosts comparably low velocities, which were initially interpreted as a face-on disk. However, low velocities have been observed in a growing sample of BCGs observed with ALMA (David et al. 2014; Russell et al. 2014, 2016; Tremblay et al. 2016), indicating that velocities well below the stellar velocity dispersion are common among BCGs. Similarly low velocities were also noted in the filamentary optical-line nebulae of BCGs (e.g., Heckman et al. 1989; Jaffe et al. 2005; Hatch et al. 2006; Oonk et al. 2010). Evidently, the gas must either be dynamically young, having not had time to settle into its gravitational potential, or the clouds are supported by pressure from either magnetic fields or the hot gas.

Redshifted CO absorption lines have been observed in NGC5044 (David et al. 2014) and A2597 (Tremblay et al. 2016). The widths of these lines are small ($\sim$5 km s^{-1}), and are comparable to individual giant molecular clouds within the Milky Way. Since the lines are seen in absorption, the clouds must lie in front of the AGN, blocking its continuum emission. The redshifted velocities indicate that the clouds are falling toward the black hole, and are possibly in the process of being accreted. The presence of both inflow and outflow in BCGs suggests that gas lifted by from the cluster core eventually returns in a circulation flow, or molecular "fountain."

The results presented here are consistent with this stimulated feedback model. *Chandra* imaging of 2A 0335+096, shown in Figure 14, reveals a series of X-ray cavities corresponding to multiple generations of AGN feedback (Mazzotta et al. 2003; Sanders et al. 2009). The Hα nebula, overlaid in white contours in Figure 14, shows a striking connection to the northwestern cavity. The emission extends from the center of the BCG directly toward the X-ray cavity identified in Figure 14, with fainter emission along the cavity's inner edge. As noted in Section 3.6, the Hα filament is coincident with soft X-ray emission from 0.5 keV gas as well as 20–30 K molecular gas. This indicates that the gas is cooling over five decades in temperature in the wake of a rising X-ray cavity. Dust grains situated along the filament have presumably been uplifted from the BCG along with the low-entropy ICM. This resembles the scene in PKS0745-191, where the two filaments trailing X-ray cavities are correlated with dust extinction. The uplifted dust potentially enhances the formation of molecular gas by offering seeding sites.

A bipolar radio jet observed at 1.5 GHz extends 12 arcsec to the northeast and southwest of the BCG (Sarazin et al. 1995; Donahue et al. 2007). This radio jet traces the most recent generation of AGN feedback, which is orthogonal to the emission-line filament. No molecular gas is observed along this direction, indicating that the radio jet itself has not disrupted the central supply of molecular gas or created thermally unstable overdensities in the hot atmosphere. Similarly, any cavities formed along this jet have yet to induce a significant amount of thermally unstable cooling.

4.2.2. Cooling Wake from Galaxy Motion

Cooling of the ICM can also be induced by the gravitational wake of a galaxy in motion with respect to the cluster. For example, A1795 hosts a BCG with a velocity of $+150$ km s^{-1} with respect to the mean of all galaxies in the cluster, or $+374$ km s^{-1} compared to the galaxies within 270 kpc (Oegerle & Hill 1994). The cluster also harbours a luminous emission-line nebula extending in a 50 kpc long filament to the southeast of the BCG (Cowie et al. 1983; Crawford et al. 2005; McDonald & Veilleux 2009). This filament has also been identified in X-ray imaging (Fabian et al. 2001; Crawford et al. 2005; Ehlert et al. 2015), molecular gas (McDonald et al. 2012), U-band polarimetry (McNamara et al. 1996), and far-UV imaging (McDonald & Veilleux 2009). Fabian et al. (2001) argued that this filament was formed from a cooling wake, where the gravitational attraction from the BCG moving through a region with a short cooling time focuses cooling onto its wake. Since the gas cools from the ICM, its velocity reflects that of the cluster instead of the BCG.

In principle either the BCG or the companion galaxy could induce this cooling wake. However, it is more likely that the BCG causes the cooling wake due to its larger gravitational attraction, provided it is in motion with respect to the ICM. Furthermore, the presence of Hα filaments in cool core clusters is not correlated with the presence of galaxies near the BCG (McDonald et al. 2010). If the companion galaxy in 2A 0335 +096 is able to induce a cooling wake, then we should expect similar filaments in all cool core clusters hosting galaxies near their core, which is evidently not the case.

Without a direct measurement of ICM velocity it is difficult to determine if the BCG is in motion with respect to the cluster. However, the X-ray atmosphere of 2A 0335+096 hosts a series of cool clumps and a cold front, which are indicative of an unrelaxed dynamical state (Mazzotta et al. 2003; Sanders et al. 2009). In particular, the X-ray centroid of the cluster is difficult to pinpoint because of the series of cool clumps. The brightest clump of X-ray emission in the 0.5–7 keV band is co-spatial with the Hα emission 6–10 kpc southeast of the BCG nucleus. The offset between the X-ray peak and the BCG, as well as the presence of sloshing motions in the ICM, suggest that the BCG is in motion relative to the cluster. We are unable to constrain the BCG velocity in this system, although sloshing motions in Virgo have velocities of $\sim$50–100 km s^{-1} (Roediger et al. 2011). The low velocity of the main component of the inner filament, -28 ± 4 km s^{-1}, may imply a small line-of-sight velocity offset between the BCG and cluster, though multiple distinct velocities throughout the filament point to a more complicated picture. Similarly, we cannot confirm that the motion is along the direction of the filament.

As noted in Section 4.1.3, gas cooling from the ICM is expected to be dust-free. This appears to be the case in A1795, where dust extinction is only observed within the central galaxy (Pinkney et al. 1996), and is likely not affecting star formation along the filament (Crawford et al. 2005). The presence of dust along the filament in 2A 0335+096 argues against the cooling wake scenario unless the filament has been enriched with dust from the BCG or companion, perhaps through ram pressure stripping. This possibility has been suggested by Sparks et al. (2004) for the filaments in M87. However, ram pressure stripping requires velocities of several hundred km s^{-1}, even in the dense cluster core.

4.2.3. Cooling Along a Dark Matter Filament

We also note an interesting similarity in the position angles of the BCG and filament and the apparent trajectory of the companion galaxy. BCGs are known to have a common orientation with their host clusters, which are themselves aligned with the cosmological filaments of dark matter they accreted from (Binggeli 1982; Niederste-Ostholt et al. 2010).

The companion galaxy may have accreted along this axis, falling from the southeast and passing through the gas supply in the BCG. Understanding how the filamentary emission is linked to the dark matter distribution is more difficult. Any overdensity caused by the filament should only be significant in the outer extent of the cluster, not in the inner tens of kpc where the emission-line nebula is observed. Direct accretion from the cosmological filament is similarly unlikely, since any accreted gas should be moving at speeds approaching the cluster velocity dispersion. The alignment noted here does not appear to persist in other cool core clusters. Perseus and Virgo, for example, harbour filamentary emission with no preferred orientation (e.g., Young et al. 2002; Salomé et al. 2006). A more likely possibility is that an infalling galaxy caused an overdensity in the ICM that led to a thermal instability. However, the only galaxy located along the filament is the companion, and it cannot produce both the disrupted central gas and the filament. Thus, the alignment between the major axis of the BCG and filament of molecular gas is most likely coincidental.

4.2.4. Summary: Cooling Origin

While stimulated cooling and the cooling wake are both feasible origins for gas condensation, we favor stimulated cooling throughout the remainder of our discussion. This is mainly because of the connection between the cooling gas and X-ray cavity, which resembles a growing sample of objects that have been observed with ALMA. As a result, stimulated cooling offers a more generally applicable explanation for the presence of molecular gas in cool core clusters.

4.3. Molecular Filament: Inflow or Outflow?

We now consider the velocity profile of the molecular filament and investigate whether it is consistent with inflow or outflow. Along the filament the gas velocity becomes increasingly blueshifted farther from the cluster center. At its base the gas is blueshifted to $-30\,\mathrm{km\,s^{-1}}$, while the velocity at the tail is nearly $-200\,\mathrm{km\,s^{-1}}$. This can be consistent with either inflow or outflow, depending on where the gas forms and where it is located along the line of sight. With the present data we are unable to conclusively distinguish between the two.

Molecular gas condensing out of the hot atmosphere should trace the velocity of the gas that it cooled from. In a cooling wake the molecular gas condenses from a hydrostatic atmosphere, resulting in a mean velocity of zero with respect to the cluster. Our adopted frame is measured with respect to the BCG, so an offset is expected if the BCG is indeed oscillating within the cluster. Molecular gas condensing from low-entropy gas lifted by an X-ray cavity should initially be flowing away from the cluster center. The observed velocity gradient then depends strongly on both the inclination of the filament as well as its shape. For example, a filament with a constant velocity may have an observed gradient if it becomes progressively more inclined toward the line of sight. We cannot differentiate between these morphologies, so preliminarily assume that the filament is straight.

Eventually the dense molecular clouds are expected to decouple from the hot atmosphere, decelerating and falling back onto the central galaxy in a circulation flow. Recent results from *Hitomi* found that the velocity of the ICM in Perseus is very similar to the cold gas, suggesting that the two phases are held together by magnetic fields for some time (Hitomi Collaboration et al. 2016). Lim et al. (2008) argued in favor of infall for the filaments nearest the cluster core based on their velocity gradient, while inflowing molecular gas was observed directly in NGC5044 (David et al. 2014) and A2597 (Tremblay et al. 2016) based on the presence of redshifted CO absorption lines. Distinguishing between inflow and outflow does not affect the consistency with the stimulated cooling model, as both are expected to occur at some point in the feedback cycle.

4.3.1. Outflow in the Wake of the Rising Cavity

If the clouds along the filament formed recently and are located in front of the midplane of the BCG, then their increasing velocity with radius implies that the gas is being accelerated away from the BCG nucleus. Localized condensation at the base of the filament followed by direct uplift of the molecular gas is unlikely, since coupling the diffuse X-ray cavity to dense molecular clouds is difficult. This is exacerbated by the high mass of the filament, so the coupling of diffuse to dense gas would need to be remarkably efficient. Instead, the molecular clouds probably condensed in situ from the uplifted, low entropy gas.

The terminal velocity of X-ray cavities is generally 50%–60% of the speed of sound, $c_s = \sqrt{\gamma kT/\mu m_{\rm H}}$, where kT is the temperature of the hot gas and we have taken $\gamma = 5/3$ for an ideal gas and $\mu = 0.62$ (e.g., Bîrzan et al. 2004). In a 3.5 keV cluster $c_s \approx 900\,\mathrm{km\,s^{-1}}$, so a typical bubble velocity is $\sim 500\,\mathrm{km\,s^{-1}}$. The molecular gas in the filament reaches a line-of-sight velocity (magnitude) of $200\,\mathrm{km\,s^{-1}}$, several times lower than the bubble velocity. In order for the two velocities to match, the filament must be inclined at $<25^\circ$ from the plane of the sky.

Accelerating the molecular gas to a speed comparable to the bubble terminal velocity of $\sim 500\,\mathrm{km\,s^{-1}}$ requires that the AGN contribute 2×10^{57} erg to the kinetic energy of the cold gas. Assuming a gravitational acceleration of $g = 2\sigma^2/r$ with $\sigma = 255\,\mathrm{km\,s^{-1}}$ (McNamara et al. 1990), the potential energy required to lift the gas from 1 kpc to $R \approx 13$ kpc is $\sim 5 \times 10^{57}$ erg. The total energy requirement is therefore $\sim 7 \times 10^{57}$ erg, which is only 4% of the enthalpy of the northwestern cavity, 1.6×10^{59} erg (Sanders et al. 2009). Lifting the molecular gas in the wake of the X-ray cavity is therefore energetically feasible.

4.3.2. Clouds in Gravitational Free-fall

When molecular clouds decouple from the hot atmosphere, they should fall ballistically under the influence of gravity. The clouds will initially have the same velocity as the hot gas they cooled from. This is zero in a hydrostatic atmosphere, but can be nonzero if the clouds have cooled from uplifted gas. Following Lim et al. (2008), we assume that the gravitational potential can be modeled by a Hernquist profile (Hernquist 1990). A gas cloud undergoing free-fall should accelerate to a velocity of

$$v(r)^2 = v(r_0)^2 + 2GM\left(\frac{1}{r+a} - \frac{1}{r_0+a}\right) \quad (3)$$

with respect to the hot atmosphere. In the rest frame of the BCG, which has been adopted for these observations, the velocities in the above equation are modified to be $v(r) - v_{\rm ICM}$,

where $v_{\rm ICM}$ is the velocity offset between the BCG and the cooling gas. We assume that the initial velocity of the cloud is the same as the ICM, so $v(r_0) = v_{\rm ICM}$. In Equation (3) M is the total gravitating mass of the BCG, a is the scale length, and r_0 is the radius where the cloud originally formed. The inclination angle of the cloud's trajectory and $v_{\rm ICM}$ are both free parameters in this model.

The scale length a is related to the half-light radius R_e according to

$$R_e \approx 1.8153a. \quad (4)$$

Taking an effective radius of 19.″24 (13.47 kpc) from the 2MASS K-band catalog, the corresponding scale length is 7.4 kpc. We note that 2MASS photometry is likely missing a significant amount of the total stellar light (Lauer et al. 2007), so this scale length is underestimated. Adopting a larger scale length would result in flatter velocity profiles.

We estimate the total BCG mass using the cluster mass profiles of Main et al. (2015), who modeled the X-ray emission of the ICM with an NFW profile under the assumption of hydrostatic equilibrium. For 2A 0335+096 the total mass interior to 30 kpc is $2.1 \times 10^{12}\,M_\odot$. Alternatively, 2MASS reports a total K-band magnitude of 9.808 ± 0.052 that was extrapolated out to 45 kpc. Assuming a K-band stellar mass-to-light ratio of 0.8 (Bell et al. 2003; Humphrey et al. 2006), the total stellar mass in the BCG of 2A 0335+096 is $4.7 \times 10^{11}\,M_\odot$. Combining these values gives a dark matter mass fraction within the BCG of 80%, which is similar to that of Hydra A at a similar radius (Okabe et al. 2016). The total gravitating mass controls the amplitude of the velocity profile, and is degenerate with the inclination angle. Our results are therefore not sensitive to the adopted value of total mass, as the inclination angle, which is not known, can be adjusted to compensate.

From the PV diagrams presented in Figure 11, infall along the extended filament begins at a radius of 11.5 kpc and proceeds over a length of 6 kpc that is oriented 20° from purely radial. The solid black line in Figure 11 shows the velocities resulting from infall along this filament assuming an inclination angle of 25° and a velocity offset of $-200\,{\rm km\,s^{-1}}$. The position shown along the x-axis has been transformed into the appropriate radial distance from the BCG nucleus. The velocity shift corresponds to a bulk offset between the ICM and the stellar component of the BCG. The presence of a cold front seen in the X-ray emission (Mazzotta et al. 2003; Werner et al. 2006; Sanders et al. 2009) indicates non-zero motion between the two components.

Over the 7 kpc length of the filament the gas is primarily located in two clumps. Gravitational free-fall reproduces the observed increase in velocity between these clumps. However, the clumps are not smoothly connected in velocity, and the free-fall model fails to account for this feature. Furthermore, the observed average velocity of the inner portion of the filament does not depend on the radius, while the velocity of the free-fall model increases linearly through this region. Although the free-fall model reproduces the bulk of the observed velocities, differences between the data and the model prevent any definitive conclusions about the gas undergoing free-fall from being drawn. Nevertheless, the velocity gradient is broadly consistent with free-fall. Since this velocity gradient is generic for free-fall in elliptical galaxies, the discovery of additional filaments exhibiting this gradient suggests that some of them, at the very least, are in approximate free-fall.

A number of additional problems with the model adopted here must also be addressed. First, the filament is not oriented radially with respect to the BCG nucleus. This may be caused by a transverse velocity offset between the ICM and the BCG, which would be expected given the presence of a cold front. This model also neglects the gravity of the companion galaxy. Assuming the companion lies in the plane of the sky and has a mass-to-light ratio comparable to the BCG, the inner portion of the filament should experience 3× more gravitational acceleration from the companion galaxy than from the BCG. This could also affect the orientation of the infalling gas. Without a reliable measurement of the line-of-sight separation between the BCG, companion galaxy, and filament, we cannot create a more robust gravitational free-fall model. Finally, the model we have adopted here has a large number of unconstrained parameters, notably the inclination angle and bulk velocity of the ICM. As a result, virtually any linear velocity structure can be reproduced with an appropriate choice of these parameters.

4.4. Star Formation

Attributing all of the Hα emission to star formation, the luminosity of $8 \times 10^{41}\,{\rm erg\,s^{-1}}$ (Donahue et al. 2007) corresponds to a star formation rate of 15–20 $M_\odot\,{\rm yr^{-1}}$, using the $L_{\rm H\alpha}$−SFR scaling relations of Kennicutt (1998). This overestimates the true star formation rate, as starlight alone fails to account for the observed spectra of emission-line nebulae (Johnstone et al. 2007). Additional heating sources are required to supplement the ionization of the nebula. Collisional heating by ionizing particles, such as cosmic rays that penetrate the filament, is favored in the models of Ferland et al. (2009). Mixing of the gas in the filaments with the hot X-ray emitting plasma was argued to provide the dominant source of heat in Virgo (Werner et al. 2013) and other ellipticals (Werner et al. 2014). The ionization source in 2A 0335+096 is not currently known, although the spatial coincidence between the filaments and 0.5 keV gas suggests that star formation alone does not power the nebula.

An analysis of the $B - I$ color gradient of the central galaxy shows an excess in blue emission from 4–30 kpc compared to the central galaxies in clusters without short cooling times (Romanishin & Hintzen 1988). This extends well beyond the companion galaxy, indicating that active star formation is occurring along the filament. Within 4 kpc the color gradient reddens to a level consistent with the control sample. Wilman et al. (2011) argued that this reddening cannot be caused by dust extinction, since any attenuation by dust would be negligible in their K-band observation. In the BCG alone, several different measurements place the star formation rate at a few $M_\odot\,{\rm yr^{-1}}$. Infrared photometry within a 6″ aperture, which excludes both the companion galaxy and the filament, derives a SFR of $2.1 M_\odot\,{\rm yr^{-1}}$ (O'Dea et al. 2008). Infrared spectroscopy (Donahue et al. 2011) and UV imaging (Donahue et al. 2007) over regions that include both galaxies but not the filament measure SFRs of 0.7 and 3–7 $M_\odot\,{\rm yr^{-1}}$, respectively.

The total molecular gas mass in the BCG is $3.2 \times 10^8\,M_\odot$. Using the CO(3–2) line to trace the emitting area yields a molecular gas surface density of $68\,M_\odot\,{\rm pc^{-2}}$. Assuming that star formation is distributed over the same area, the maximum SFR to place the 2A 0335+096 BCG within the scatter of the Kennicutt–Schmidt relation (Kennicutt 1998; Kennicutt &

Evans 2012) is $\sim 0.9\,M_{\odot}\,\mathrm{yr}^{-1}$. The SFR derived from IR spectroscopy is consistent with this limit. For the $7.8 \times 10^{8}\,M_{\odot}$ of molecular gas in the filament, the corresponding surface density of molecular gas is $46\,M_{\odot}\,\mathrm{pc}^{-2}$. Placing this on the Kennicutt–Schmidt relation requires an SFR of roughly $0.09\,M_{\odot}\,\mathrm{yr}^{-1}$. However, the low confining pressure of the ICM outside of the cluster core reduces the star formation efficiency in systems with similar filaments (e.g., Verdugo et al. 2015; Salomé et al. 2016a, 2016b). We should therefore expect a lower SFR, although the excess blue emission still supports ongoing star formation within the filament.

5. CONCLUSIONS

In this work we have presented ALMA observations of the CO(1–0) and CO(3–2) lines of the 2A 0335+096 BCG. We detect $1.13 \times 10^{9}\,M_{\odot}$ of molecular gas that is distributed between two distinct structures: a component near the center of the BCG and a 7 kpc long filament beginning 6 kpc from the BCG nucleus and extending nearly radially outward. Most of the molecular gas, $7.8 \times 10^{8}\,M_{\odot}$, is located in the filament, while $3.2 \times 10^{8}\,M_{\odot}$ is located in the nucleus. The nuclear gas is highly asymmetric, with two clumps of comparable mass south of the radio source and several smaller clouds extending toward a nearby companion galaxy. The filament has a shallow velocity gradient that is slightly blueshifted at all points, nearing the systemic velocity of the BCG at its innermost radius. No molecular gas is detected connecting the filament to the BCG nucleus.

Although a companion galaxy is located 5 kpc from the BCG in projection and has a small relative velocity ($\sim 200\,\mathrm{km\,s}^{-1}$), it is unlikely that the molecular gas has been supplied by a merger. Tidal stripping alone could deposit molecular gas onto the BCG, but the filament must then form via completely independent means. A plume of increasingly redshifted clouds extending toward the companion galaxy suggests that the galaxies have already interacted, with the companion galaxy disrupting a pre-existing reservoir of molecular gas within the BCG as it passed through the nucleus at $<$20Myr ago. However, no evidence of stellar disruption is observed in optical imaging, indicating that any tidal interaction must be weak.

Ram pressure stripping is a feasible way to produce the filament, as similar structures have been observed in other systems (e.g., ESO 137-01). However, filamentary emission has also been observed in a number of cool core clusters that do not have nearby companion galaxies. While we cannot definitively rule out ram pressure stripping, it is not representative of cool core clusters in general. Moreover, if the galaxies have already interacted, then ram pressure stripping cannot be a viable mechanism for producing the filament.

The filament of molecular gas is coincident with significant dust extinction, luminous Hα emission, and 0.5 keV X-ray emitting gas. This spatial correlation of gas spanning 5–6 decades in temperature implies that the molecular gas has condensed out of gas cooling from the hot atmosphere. The hot atmosphere offers an abundant source of gas with which to form the molecular gas. Condensation out of the hot atmosphere can form the total molecular gas supply rapidly enough to sustain cycles of AGN feedback every $\sim 10^{8}$ years. Condensation can be triggered either in the wake of the BCG or in the uplift behind an X-ray cavity. We favor the uplift interpretation because of its similarity to a growing sample of objects observed with ALMA, which may be representative of cool core clusters in general.

The Hα emission from this cooling filament extends toward an X-ray cavity, with faint emission spreading around its inner edge. This resembles the distribution of molecular gas in a growing number of objects observed with ALMA (e.g., PKS0745-191 and A1835), where significant amounts of molecular gas reside in massive outflows linked to the buoyantly rising X-ray cavities. Our observations are consistent with the "stimulated feedback" model, where molecular gas condenses out of low-entropy gas that is lifted out of thermal equilibrium by X-ray cavities. With an enthalpy of 1.6×10^{59} erg, the X-ray cavity possesses ample energy to lift enough low-entropy gas to form the observed molecular gas supply.

As clouds of molecular gas condense out of the uplifted low-entropy gas in the hot atmosphere, they should decouple from the hot atmosphere and fall back onto the BCG under the influence of gravity. Initially outflowing gas will eventually decelerate and return to the BCG in an inflow. We are unable to distinguish between inflow and outflow with our observations. The velocity of the molecular gas in the filament increases in magnitude from $-30\,\mathrm{km\,s}^{-1}$ near its base to $-200\,\mathrm{km\,s}^{-1}$ at its tail. This velocity gradient may correspond to gas accelerated by the cavity, but is also consistent with simple models of gravitational infall. This ambiguity, however, does not affect our interpretation that the molecular gas has condensed out of low-entropy gas uplifted by an X-ray cavity.

We thank the anonymous referee for helpful comments that improved this paper. Support for this work was provided in part by the National Aeronautics and Space Administration through Chandra Award Number G05-16134X issued by the Smithsonian Astrophysical Observatory for an on behalf of the National Aeronautics and Space Administration under contract NAS8-03060. A.N.V. and B.R.M. acknowledge support from the Natural Sciences and Engineering Research Council of Canada. B.R.M. further acknowledges support from the Canadian Space Agency Space Science Enhancement Program. A.C.F. and H.R.R. acknowledge support from ERC Advanced Grant Feedback 340442. This paper makes use of the following ALMA data: ADS/JAO.ALMA 2012.1.00837.S. ALMA is a partnership of the ESO (representing its member states), NSF (USA) and NINS (Japan), together with NRC (Canada), NSC and ASIAA (Taiwan), and KASI (Republic of Korea), in cooperation with the Republic of Chile. The Joint ALMA Observatory is operated by ESO, AUI/NRAO, and NAOJ. This research made use of Astropy, a community-developed core Python package for Astronomy (Astropy Collaboration, 2013). This research made use of APLpy, an open-source plotting package for Python hosted at http://aplpy.github.com.

REFERENCES

Alatalo, K., Blitz, L., Young, L. M., et al. 2011, ApJ, 735, 88
Bell, E. F., McIntosh, D. H., Katz, N., & Weinberg, M. D. 2003, ApJS, 149, 289
Binggeli, B. 1982, A&A, 107, 338
Bîrzan, L., Rafferty, D. A., McNamara, B. R., Wise, M. W., & Nulsen, P. E. J. 2004, ApJ, 607, 800
Blanton, E. L., Sarazin, C. L., McNamara, B. R., & Wise, M. W. 2001, ApJL, 558, L15
Bolatto, A. D., Wolfire, M., & Leroy, A. K. 2013, ARA&A, 51, 207

Cardelli, J. A., Clayton, G. C., & Mathis, J. S. 1989, ApJ, 345, 245
Cavagnolo, K. W., Donahue, M., Voit, G. M., & Sun, M. 2008, ApJL, 683, L107
Cowie, L. L., Hu, E. M., Jenkins, E. B., & York, D. G. 1983, ApJ, 272, 29
Crawford, C. S., Sanders, J. S., & Fabian, A. C. 2005, MNRAS, 361, 17
David, L. P., Lim, J., Forman, W., et al. 2014, ApJ, 792, 94
di Serego Alighieri, S., Gavazzi, G., Giovanardi, C., et al. 2007, A&A, 474, 851
Donahue, M., Connor, T., Fogarty, K., et al. 2015, ApJ, 805, 177
Donahue, M., de Messières, G. E., O'Connell, R. W., et al. 2011, ApJ, 732, 40
Donahue, M., Sun, M., O'Dea, C. P., Voit, G. M., & Cavagnolo, K. W. 2007, AJ, 134, 14
Donahue, M., & Voit, G. M. 1993, ApJL, 414, L17
Draine, B. T., & Salpeter, E. E. 1979, ApJ, 231, 77
Dunn, R. J. H., & Fabian, A. C. 2006, MNRAS, 373, 959
Edge, A. C. 2001, MNRAS, 328, 762
Edge, A. C., & Frayer, D. T. 2003, ApJL, 594, L13
Edge, A. C., Stewart, G. C., Fabian, A. C., & Arnaud, K. A. 1990, MNRAS, 245, 559
Egami, E., Misselt, K. A., Rieke, G. H., et al. 2006, ApJ, 647, 922
Ehlert, S., McDonald, M., David, L. P., Miller, E. D., & Bautz, M. W. 2015, ApJ, 799, 174
Fabian, A. C. 1994, ARA&A, 32, 277
Fabian, A. C. 2012, ARA&A, 50, 455
Fabian, A. C., Johnstone, R. M., Sanders, J. S., et al. 2008, Natur, 454, 968
Fabian, A. C., Sanders, J. S., Crawford, C. S., et al. 2003, MNRAS, 344, L48
Fabian, A. C., Sanders, J. S., Ettori, S., et al. 2001, MNRAS, 321, L33
Fabian, A. C., Sanders, J. S., Taylor, G. B., et al. 2006, MNRAS, 366, 417
Farage, C. L., McGregor, P. J., & Dopita, M. A. 2012, ApJ, 747, 28
Ferland, G. J., Fabian, A. C., Hatch, N. A., et al. 2009, MNRAS, 392, 1475
Gaspari, M., Ruszkowski, M., & Oh, S. P. 2013, MNRAS, 432, 3401
Gaspari, M., Ruszkowski, M., & Sharma, P. 2012, ApJ, 746, 94
Gelderman, R. 1996, in ASP Conf. Ser. 88, Clusters, Lensing, and the Future of the Universe, ed. V. Trimble & A. Reisenegger (San Francisco, CA: ASP), 168
Graham, A. W., Erwin, P., Trujillo, I., & Asensio Ramos, A. 2003, AJ, 125, 2951
Grossi, M., di Serego Alighieri, S., Giovanardi, C., et al. 2009, A&A, 498, 407
Hatch, N. A., Crawford, C. S., & Fabian, A. C. 2007, MNRAS, 380, 33
Hatch, N. A., Crawford, C. S., Johnstone, R. M., & Fabian, A. C. 2006, MNRAS, 367, 433
Häußler, B., Bamford, S. P., Vika, M., et al. 2013, MNRAS, 430, 330
Haynes, M. P., Giovanelli, R., & Chincarini, G. L. 1984, ARA&A, 22, 445
Heckman, T. M. 1981, ApJL, 250, L59
Heckman, T. M., Baum, S. A., van Breugel, W. J. M., & McCarthy, P. 1989, ApJ, 338, 48
Hernquist, L. 1990, ApJ, 356, 359
Hitomi Collaboration, Aharonian, F., Akamatsu, H., et al. 2016, Natur, 535, 117
Hogan, M. T., Edge, A. C., Geach, J. E., et al. 2015, MNRAS, 453, 1223
Hu, E. M., Cowie, L. L., & Wang, Z. 1985, ApJS, 59, 447
Huchra, J. P., Macri, L. M., Masters, K. L., et al. 2012, ApJS, 199, 26
Humphrey, P. J., Buote, D. A., Gastaldello, F., et al. 2006, ApJ, 646, 899
Jáchym, P., Combes, F., Cortese, L., Sun, M., & Kenney, J. D. P. 2014, ApJ, 792, 11
Jaffe, W., Bremer, M. N., & Baker, K. 2005, MNRAS, 360, 748
Johnstone, R. M., Hatch, N. A., Ferland, G. J., et al. 2007, MNRAS, 382, 1246
Kenney, J. D. P., & Young, J. S. 1989, ApJ, 344, 171
Kennicutt, R. C., & Evans, N. J. 2012, ARA&A, 50, 531
Kennicutt, R. C., Jr. 1998, ARA&A, 36, 189
Kinney, A. L., Calzetti, D., Bohlin, R. C., et al. 1996, ApJ, 467, 38
Kormendy, J., Fisher, D. B., Cornell, M. E., & Bender, R. 2009, ApJS, 182, 216
Lauer, T. R., Faber, S. M., Richstone, D., et al. 2007, ApJ, 662, 808
Lavaux, G., & Hudson, M. J. 2011, MNRAS, 416, 2840
Li, Y., & Bryan, G. L. 2014a, ApJ, 789, 54
Li, Y., & Bryan, G. L. 2014b, ApJ, 789, 153
Lim, J., Ao, Y., & Dinh-V-Trung 2008, ApJ, 672, 252
Lim, J., Ohyama, Y., Chi-Hung, Y., Dinh-V-Trung, & Shiang-Yu, W. 2012, ApJ, 744, 112
Main, R., McNamara, B., Nulsen, P., Russell, H., & Vantyghem, A. 2015, arXiv:1510.07046
Mazzotta, P., Edge, A. C., & Markevitch, M. 2003, ApJ, 596, 190
McDonald, M., & Veilleux, S. 2009, ApJL, 703, L172
McDonald, M., Veilleux, S., & Rupke, D. S. N. 2012, ApJ, 746, 153
McDonald, M., Veilleux, S., Rupke, D. S. N., & Mushotzky, R. 2010, ApJ, 721, 1262
McDonald, M., Veilleux, S., Rupke, D. S. N., Mushotzky, R., & Reynolds, C. 2011, ApJ, 734, 95
McMullin, J. P., Waters, B., Schiebel, D., Young, W., & Golap, K. 2007, in ASP Conf. Ser. 376, Astronomical Data Analysis Software and Systems XVI, ed. R. A. Shaw, F. Hill, & D. J. Bell (San Francisco, CA: ASP), 127
McNamara, B. R. 2004, in The Riddle of Cooling Flows in Galaxies and Clusters of Galaxies, ed. T. Reiprich, J. Kempner, & N. Soker (Charlottesville, VA: Univ. Virginia), 177
McNamara, B. R., Jannuzi, B. T., Elston, R., Sarazin, C. L., & Wise, M. 1996, ApJ, 469, 66
McNamara, B. R., Kazemzadeh, F., Rafferty, D. A., et al. 2009, ApJ, 698, 594
McNamara, B. R., & Nulsen, P. E. J. 2007, ARA&A, 45, 117
McNamara, B. R., & Nulsen, P. E. J. 2012, NJPh, 14, 055023
McNamara, B. R., O'Connell, R. W., & Bregman, J. N. 1990, ApJ, 360, 20
McNamara, B. R., Russell, H. R., Nulsen, P. E. J., et al. 2014, ApJ, 785, 44
McNamara, B. R., Russell, H. R., Nulsen, P. E. J., et al. 2016, arXiv:1604.04629
McNamara, B. R., Wise, M., Nulsen, P. E. J., et al. 2000, ApJL, 534, L135
Morganti, R., Oosterloo, T., Oonk, J. B. R., Frieswijk, W., & Tadhunter, C. 2015, A&A, 580, A1
Morganti, R., Tadhunter, C. N., & Oosterloo, T. A. 2005, A&A, 444, L9
Nesvadba, N. P. H., Lehnert, M. D., Eisenhauer, F., et al. 2006, ApJ, 650, 693
Niederste-Ostholt, M., Strauss, M. A., Dong, F., Koester, B. P., & McKay, T. A. 2010, MNRAS, 405, 2023
Nulsen, P. E. J. 1986, MNRAS, 221, 377
O'Dea, C. P., Baum, S. A., & Gallimore, J. F. 1994, ApJ, 436, 669
O'Dea, C. P., Baum, S. A., Privon, G., et al. 2008, ApJ, 681, 1035
Oegerle, W. R., & Hill, J. M. 1994, AJ, 107, 857
Okabe, N., Umetsu, K., Tamura, T., et al. 2016, MNRAS, 456, 4475
Oonk, J. B. R., Jaffe, W., Bremer, M. N., & van Weeren, R. J. 2010, MNRAS, 405, 898
Peng, C. Y., Ho, L. C., Impey, C. D., & Rix, H.-W. 2002, AJ, 124, 266
Peng, C. Y., Ho, L. C., Impey, C. D., & Rix, H.-W. 2010, AJ, 139, 2097
Peterson, J. R., & Fabian, A. C. 2006, PhR, 427, 1
Pinkney, J., Holtzman, J., Garasi, C., et al. 1996, ApJL, 468, L13
Pizzolato, F., & Soker, N. 2005, ApJ, 632, 821
Poggianti, B. M. 1997, A&AS, 122, 399
Protassov, R., van Dyk, D. A., Connors, A., Kashyap, V. L., & Siemiginowska, A. 2002, ApJ, 571, 545
Rafferty, D. A., McNamara, B. R., & Nulsen, P. E. J. 2008, ApJ, 687, 899
Rafferty, D. A., McNamara, B. R., Nulsen, P. E. J., & Wise, M. W. 2006, ApJ, 652, 216
Reiprich, T. H., & Böhringer, H. 2002, ApJ, 567, 716
Revaz, Y., Combes, F., & Salomé, P. 2008, A&A, 477, L33
Roediger, E., Brüggen, M., Simionescu, A., et al. 2011, MNRAS, 413, 2057
Romanishin, W., & Hintzen, P. 1988, ApJL, 324, L17
Russell, H. R., McNamara, B. R., Edge, A. C., et al. 2014, ApJ, 784, 78
Russell, H. R., McNamara, B. R., Fabian, A. C., et al. 2016, arXiv:1602.05962
Salomé, P., & Combes, F. 2003, A&A, 412, 657
Salomé, P., Combes, F., Edge, A. C., et al. 2006, A&A, 454, 437
Salomé, P., Combes, F., Revaz, Y., et al. 2008, A&A, 484, 317
Salomé, P., Combes, F., Revaz, Y., et al. 2011, A&A, 531, A85
Salomé, Q., Salomé, P., Combes, F., & Hamer, S. 2016a, arXiv:1605.05986
Salomé, Q., Salomé, P., Combes, F., Hamer, S., & Heywood, I. 2016b, A&A, 586, A45
Sanders, J. S., Fabian, A. C., & Taylor, G. B. 2009, MNRAS, 396, 1449
Sarazin, C. L., Baum, S. A., & O'Dea, C. P. 1995, ApJ, 451, 125
Schlafly, E. F., & Finkbeiner, D. P. 2011, ApJ, 737, 103
Schwartz, D. A., Schwarz, J., & Tucker, W. 1980, ApJL, 238, L59
Singh, K. P., Westergaard, N. J., & Schnopper, H. W. 1986, ApJL, 308, L51
Singh, K. P., Westergaard, N. J., & Schnopper, H. W. 1988, ApJ, 331, 672
Solomon, P. M., Rivolo, A. R., Barrett, J., & Yahil, A. 1987, ApJ, 319, 730
Solomon, P. M., & Vanden Bout, P. A. 2005, ARA&A, 43, 677
Sparks, W. B., Donahue, M., Jordán, A., Ferrarese, L., & Côté, P. 2004, ApJ, 607, 294
Sun, M., Jones, C., Forman, W., et al. 2006, ApJL, 637, L81
Tonnesen, S., Bryan, G. L., & Chen, R. 2011, ApJ, 731, 98
Tremblay, G. R., O'Dea, C. P., Baum, S. A., et al. 2015, MNRAS, 451, 3768
Tremblay, G. R., Oonk, J. B. R., Combes, F., et al. 2016, Natur, 534, 218
Ueda, J., Iono, D., Yun, M. S., et al. 2014, ApJS, 214, 1
Vantyghem, A. N., McNamara, B. R., Russell, H. R., et al. 2014, MNRAS, 442, 3192
Verdugo, C., Combes, F., Dasyra, K., Salomé, P., & Braine, J. 2015, A&A, 582, A6

Villar-Martín, M., Sánchez, S. F., De Breuck, C., et al. 2006, MNRAS, 366, L1
Voit, G. M., Cavagnolo, K. W., Donahue, M., et al. 2008, ApJL, 681, L5
Voit, G. M., & Donahue, M. 2015, ApJL, 799, L1
Vollmer, B., Braine, J., Pappalardo, C., & Hily-Blant, P. 2008, A&A, 491, 455
Werner, N., de Plaa, J., Kaastra, J. S., et al. 2006, A&A, 449, 475
Werner, N., Oonk, J. B. R., Canning, R. E. A., et al. 2013, ApJ, 767, 153
Werner, N., Oonk, J. B. R., Sun, M., et al. 2014, MNRAS, 439, 2291
Whiley, I. M., Aragón-Salamanca, A., De Lucia, G., et al. 2008, MNRAS, 387, 1253
White, D. A., Fabian, A. C., Johnstone, R. M., Mushotzky, R. F., & Arnaud, K. A. 1991, MNRAS, 252, 72
Wilman, R. J., Edge, A. C., McGregor, P. J., & McNamara, B. R. 2011, MNRAS, 416, 2060
Young, A. J., Wilson, A. S., & Mundell, C. G. 2002, ApJ, 579, 560
Young, L. M., Bureau, M., Davis, T. A., et al. 2011, MNRAS, 414, 940